

Chance Constrained PDE-Constrained Optimal Design Strategies Under High-Dimensional Uncertainty

Pratyush Kumar Singh^a, Danial Faghihi^{a,*}

^a*Department of Mechanical and Aerospace Engineering, University at Buffalo, Buffalo, NY, USA*

Abstract

This study presents an advanced computational framework for the optimal design of thermal insulation components in buildings, utilizing silica aerogel porous materials. The framework aims to achieve superior thermal insulation while maintaining structural integrity of the component under stress concentrations. A multiphase continuum model is employed to simulate the thermomechanical behavior of the insulation system, governed by a set of coupled partial differential equations (PDEs). The design process explicitly accounts for spatially correlated uncertainties in the design parameters, particularly the spatially varying aerogel porosity, resulting in a high-dimensional, PDE-constrained optimization under uncertainty. The optimization problem is formulated using a risk-averse cost functional to balance insulation performance with uncertainty mitigation, incorporating statistical moments of the design objective. Additionally, chance constraints are imposed to limit the probability of stress exceeding critical thresholds. To address the challenges arising from high-dimensional parameters, the optimization leverages a second-order Taylor expansion of both the design objective and the chance constraint functions, combined with a low-rank approximation of the Hessian matrix for efficient evaluation of the generalized eigenvalue problem. This approach supports scalable computations, either directly or as a variance-reduction control variate for Monte Carlo estimations. Combined with a gradient-based optimization approach, we achieve a scalable solution algorithm with dimension-independent computational costs in terms of number of PDE solved. Two- and three-dimensional numerical experiments on the design of thermal breaks in buildings showcase the features of the proposed

*Corresponding Author, daniaalfa@buffalo.edu (D. Faghihi)

design under uncertainty framework with respect to accuracy, scalability, and computational cost.

Keywords: Thermal insulation, Optimal design, PDE-constrained optimization, chance constraint, high-dimensional parameters, uncertainty quantification

1. Introduction

Silica aerogels have emerged as a premier class of porous materials for high-performance thermal insulation, widely utilized across diverse engineering applications due to their exceptionally low thermal conductivity [1, 2, 3]. Among these applications, aerogel-based insulation components for building envelopes hold significant promise, offering the potential to enhance energy efficiency, reduce carbon emissions, and promote environmental sustainability. However, the adoption of silica aerogels in such systems is hindered by their inherently low mechanical strength and susceptibility to failure under localized stress concentrations. Recent advancements in extrusion-based additive manufacturing may be able to address these limitations by enabling precise spatial control over material deposition, thereby enhancing the mechanical stability of components. These developments have paved the way for integrating silica aerogels into lightweight thermal break insulation elements [2, 4], which effectively interrupt heat transfer pathways and mitigate the adverse effects of thermal bridging at assembly interfaces [5, 6]. Nevertheless, significant uncertainties remain regarding the thermal and mechanical performance of additively manufactured aerogel components, posing challenges to their adoption as reliable and sustainable solutions for thermal break applications in building envelopes.

In recent years, significant efforts have been dedicated to developing computational methods for topology optimization governed by partial differential equations (PDEs) (e.g., [7, 8, 9, 10, 11, 12, 13, 14, 15]). However, the optimal design of additively manufactured aerogel thermal breaks poses two major computational challenges. The first challenge arises from uncertainties in design parameters, stemming from variations in material properties, external loads, and environmental conditions. In particular, the layer-by-layer manufacturing process of aerogel components introduces spatially correlated uncertainties along the layer deposition direction, necessitating the representation of these uncertainties as spatially varying random fields. When discretized,

the resulting high-dimensional parameter space makes the optimization problem computationally prohibitive due to the “curse of dimensionality” and the need for repeated evaluations of nonlinear PDEs governing material behavior. The second challenge involves incorporating stress constraints into the optimization process, which introduces nonlinearity and numerical instability. Stress gradients often exhibit discontinuities, further complicating the numerical implementation. To mitigate these issues, global stress constraints that aggregate stress measures (e.g., von Mises stress) across the design domain are commonly employed, significantly reducing the number of constraints. However, selecting an efficient stress aggregation function with appropriate parameters is crucial to achieving computational efficiency while ensuring the detection of localized stress concentrations. Furthermore, stress measures are influenced by uncertainties in material properties and operating conditions, necessitating the incorporation of randomness into stress constraints during the optimization process.

To address uncertainty in optimization, one approach is to utilize a risk-averse formulation of the cost functional, that takes into account the statistical moments of the objective, e.g., [16, 17, 18, 19, 20, 21, 22, 11, 23, 24]. However, these methods face significant computational challenges when evaluating the statistical properties of objectives or conditional probabilities, especially in the context of PDE-constrained optimization within high-dimensional parameter spaces. Various approximations have been proposed to address these challenges. Ghattas et al. [25, 20, 19, 18] utilized Taylor expansions for scalable, dimension-independent solutions with significant computational savings. This linearization, previously applied in robust design [26, 27] and topology optimization [28], was extended by Kriegesmann et al. [21, 29, 30] with a first-order second-moment method for efficient variance gradient evaluation. Tan et al. [31] extended the Taylor approximation method to a multi-objective PDE-constrained optimization framework for multi-material systems under uncertainty. Their approach incorporates phase-field regularization to effectively manage spatial sparsity and the material interface. Chen and Royset [32] provided further analysis of approximation-based algorithms for PDE-constrained optimization under uncertainty. In the context of stress constraints, several studies have investigated the integration of these constraints into optimization frameworks for diverse materials and manufacturing processes [33, 34, 35, 36, 37, 14, 38, 39, 40, 41]. Significant efforts have also focused on incorporating uncertainty into stress-constrained optimization [42], addressing factors such as variable

loading and heat sources. For instance, Silva et al. [35] developed a method to account for uncertainties in boundary conditions during manufacturing. Similarly, Oh et al. [43] proposed a topology optimization approach that incorporates uncertainties in loading positions.

Building on previous work, this study presents a scalable computational framework for risk-averse PDE-constrained optimization under spatially correlated and high-dimensional uncertainty, while incorporating chance constraints. The framework is applied to the design of thermal breaks in building envelope, aiming to maximize thermal insulation performance and ensure mechanical stability by mitigating stress concentrations through chance constraints. The forward model is based on a thermomechanical continuum mixture theory for porous materials. The PDE model parameters, such as solid and fluid conductivities and solid elastic modulus, have been determined through model calibration in prior studies. Material porosity, modeled as a spatially correlated random field, serves as the design parameter. Discretization of this field transforms the problem into a high-dimensional optimization under uncertainty. To achieve target performance levels while mitigating the uncertainty, the framework employs a risk-averse formulation that integrates the mean and variance of the design objective. The computational burden of Monte Carlo moment estimation is mitigated using second-order Taylor approximations for the design objective and chance constraints. An inexact Newton-Conjugate Gradient algorithm with convergence properties independent of problem dimension is utilized to ensure computational scalability—measured by the number of PDE solutions—regardless of the dimensionality of the design parameter space. The effectiveness and computational cost of the framework are explored through two- and three-dimensional numerical examples, including a case study of a beam-thermal break component in the building envelope. Compared to our earlier work in [31], the key contributions of this study are as follows: (1) Incorporation of probabilistic constraints in the optimization framework to mitigate stress concentrations. (2) Utilization of second-order Taylor approximations as a control variate for Monte Carlo estimation of the design objective, enabling more accurate optimal designs in high-variance uncertainty scenarios. (3) Implementation of an inexact Newton-Conjugate Gradient algorithm, facilitating parallelization and accelerating PDE-constrained optimization calculations. (4) Extension of the numerical framework to three-dimensional design of insulation components.

The rest of the paper is organized as follows: Section 2 presents the

optimal design under uncertainty problem, including the thermomechanical forward model, the modeling of spatially correlated uncertainty in the design parameter, and the formulation of mean-variance optimization. Section 3 is dedicated to the approximation methods, encompassing Taylor approximation and the Monte Carlo estimate with control variate of the moments of the design objective. Section 4 describes the gradient-based optimization method and explains the computation of the gradient of the cost functional concerning the design parameter. Section 5 presents the numerical experiments on the optimal design of thermal breaks, followed by the conclusions and future works in Section 6.

2. Problem formulation: Design of aerogel thermal break under uncertainty

This study investigates the optimal design of building insulation components using silica aerogel materials. Figure 1 illustrates the schematic representation of a building thermal break, consisting of a concrete beam integrated with an aerogel insulation system, along with the thermal and mechanical boundary conditions employed in the numerical experiments. Concrete beams significantly influence the thermal performance of building envelopes due to their high thermal conductivity, which creates preferential pathways for heat transfer. The inclusion of silica aerogel thermal breaks disrupts this conduction, effectively mitigating thermal bridging from the interior to the exterior of the building envelope. However, thermal expansion of the concrete beam can induce stress concentrations within the silica aerogel insulation component, potentially leading to mechanical failure and compromising the thermal break’s effectiveness. In this section, we introduce the problem of optimal design under uncertainty, leveraging a forward model of aerogel and concrete materials governed by a system of partial differential equations (PDEs). We then describe how the uncertainty in design parameters are modeled, as well as formulation of design problem.

2.1. Forward thermomechanical model and design objectives

For silica aerogel materials, we utilize a thermomechanical model based on continuum mixture theory [44]. The model accounts for both an incompressible solid aerogel phase and a compressible fluid (gaseous) phase within the material. According to the mixture theory, each phase independently adheres to its own motion, balance laws, internal energy, and entropy, while

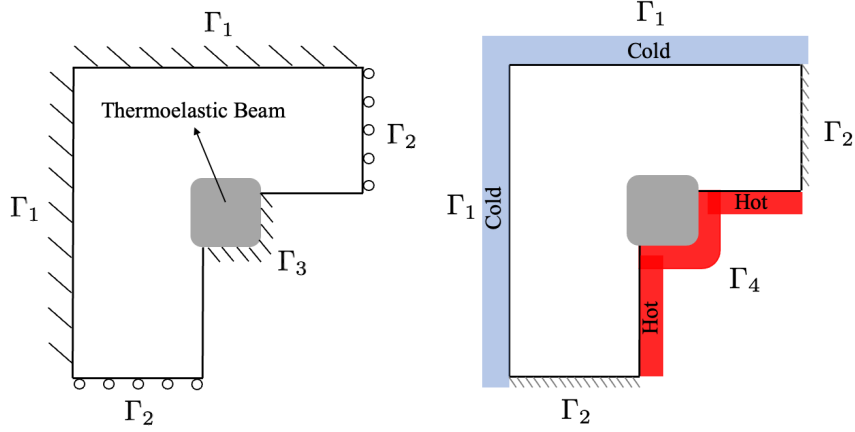


Figure 1: The domain of a beam-insulator system used for numerical experiments, indicating both the mechanical (left) and thermal (right) boundary conditions.

collectively following the overall balance laws governing the entire mixture. As a result, a system of four partial differential equations is derived, which governs the heat transfer in the solid and fluid phases, and the deformation in the solid phase and the evolution of pore pressure. For our problem of designing thermal breaks, we focus on steady-state and static conditions, which simplify the governing equations to the following PDEs,

$$\begin{cases} -\nabla \cdot (\phi_s \kappa_s \nabla \theta_s) + h(\theta_s - \theta_f) = 0 & \text{in } \Omega, \\ -\nabla \cdot (\phi_f \kappa_f \nabla \theta_f) - h(\theta_s - \theta_f) = 0 & \text{in } \Omega, \\ -\phi_s \kappa_s \nabla \theta_s = h_{\text{air}}(\theta_s - \theta_{\text{amb}}) & \text{on } \Gamma_1 \cup \Gamma_4, \\ -\phi_f \kappa_f \nabla \theta_f = h_{\text{air}}(\theta_f - \theta_{\text{amb}}) & \text{on } \Gamma_1 \cup \Gamma_4, \end{cases} \quad (1)$$

$$\begin{cases} Dp + (\nabla \cdot \mathbf{u}_s) = 0 & \text{in } \Omega, \\ -\nabla \cdot \mathbf{T}'_s - (2\phi_f - 1)\nabla p = 0 & \text{in } \Omega, \\ \mathbf{u}_s = \bar{\mathbf{u}}_s & \text{on } \Gamma_1 \cup \Gamma_3, \\ \nabla \mathbf{u}_s \cdot \mathbf{n} = 0 & \text{on } \Gamma_2 \end{cases} \quad (2)$$

where model parameters are $\theta = (\kappa_s, \kappa_f, D, \mathbf{E}_s)$ and states are $u = (\theta_s, \theta_f, \mathbf{u}_s, p)$. The state variables θ_s , θ_f , \mathbf{u}_s , and p represent the solid and fluid temperatures, solid displacement, and fluid pressure, respectively, defined over the domain Ω . Here, $\phi_f(\mathbf{x})$ represents the volume fraction of fluid (porosity), and $\phi_s(\mathbf{x})$ represents the volume fraction of solid, which can alternatively be

written as $1 - \phi_f(\mathbf{x})$. The solid displacement is subject to fixed values $\bar{\mathbf{u}}_s$ at the boundaries Γ_1 and Γ_3 . A roller boundary condition is implemented at Γ_2 . At Γ_1 and Γ_4 , we consider convective heat transfer with a coefficient h_{air} and ambient temperature θ_{amb} . A Neumann type boundary condition with no heat flux is implemented at Γ_2 . In the above equations, $\Omega \subset \mathbb{R}^d$ is an open and bounded domain with Lipschitz boundary $\partial\Omega$, and $\Gamma_1, \Gamma_3, \Gamma \subset \partial\Omega$ denote the Dirichlet and $\Gamma_2 \subset \partial\Omega$ indicate the Neumann portions of $\partial\Omega$ such that $\Gamma_1 \cup \Gamma_2 \cup \Gamma_4 = \partial\Omega$, $\Gamma_1 \cap \Gamma_2 = \emptyset$, $\Gamma_3 \cap \Gamma_4 = \Gamma_3$, and $\Gamma_1 \cap \Gamma_4 = \emptyset$. In (2), the effective solid stress is

$$\mathbf{T}'_s = 2\mu \mathbf{E}_s + \lambda \text{tr}(\mathbf{E}_s) \mathbf{I} \quad \text{with} \quad \mathbf{E}_s = \frac{1}{2}(\nabla \mathbf{u}_s + (\nabla \mathbf{u}_s)^T), \quad (3)$$

where \mathbf{E}_s is the solid strain and λ and μ are the Lamé constants. Determining the model parameters $\kappa_s, \kappa_f, h, K, C$, and μ from experimental data of silica aerogel is demonstrated in [45] and assumed to be known. for the concrete beam we consider the following thermoelastic model,

$$\begin{cases} -\nabla \cdot (\kappa_b \nabla \theta_b) = 0 & \text{in } \Omega_b, \\ \kappa_b \nabla \theta_b = h_{\text{air}}(\theta_b - \theta_{\text{amb}}) & \text{on } \Gamma_3, \\ \nabla \cdot \mathbf{T}_b = 0 & \text{in } \Omega_b \end{cases} \quad (4)$$

where κ_b is thermal conductivity of beam, θ_b represents temperature of beam and \mathbf{T}_b is the beam stress. In (4), the stress in beam is

$$\mathbf{T}_b = 2\mu_b \mathbf{E}_b + \lambda_b \text{tr}(\mathbf{E}_b) \mathbf{I} - \alpha_T (3\lambda_b + 2\mu_b)(\theta_b - \theta_0) \quad \text{with} \quad \mathbf{E}_b = \frac{1}{2}(\nabla \mathbf{u}_b + (\nabla \mathbf{u}_b)^T) \quad (5)$$

where \mathbf{E}_b is strain in the beam, and λ_b and μ_b are the Lamé constants for the beam, α_T is coefficient of thermal expansion and θ_0 is the reference temperature.

In the following sections, the forward state problems (1), (2) and (4) are expressed in an abstract form as,

$$\mathcal{R}(\mathbf{u}, m, d) = 0 \quad \text{in } \mathcal{V}', \quad (6)$$

where, given the uncertain parameter $m \in \mathcal{M}$ and design parameter $d \in \mathcal{D}$, the goal is to find the state $\mathbf{u} = (\theta_s, \theta_f, \mathbf{u}_s, p, \mathbf{u}_b) \in \mathcal{U}$ such that the PDE residual operator $\mathcal{R}(\cdot)$ is minimized to zero in \mathcal{V}' . Here \mathcal{M} and \mathcal{D} represent

infinite-dimensional Hilbert spaces, and \mathcal{V}' denotes the corresponding dual space.

Weak formulation. To derive the weak formulation of the governing equations, we start with the partial differential equations (PDEs) (1), (2) and (4). The problem can be stated as follows: *Find* $\mathbf{u} = (\theta_s, \theta_f, \theta_b, \mathbf{u}_s, \mathbf{u}_b, p) \in \mathcal{U}$, *such that*

$$\begin{aligned} -\langle \phi_s \kappa_s \nabla \theta_s, \nabla z_s \rangle - \langle h(\theta_s - \theta_f), z_s \rangle - \langle \phi_s h_{\text{air}}(\theta_s - \theta_{\text{amb}}), z_s \rangle &= 0, \\ -\langle \phi_f \kappa_f \nabla \theta_f, \nabla z_f \rangle + \langle h(\theta_f - \theta_b), z_f \rangle - \langle \phi_f h_{\text{air}}(\theta_f - \theta_{\text{amb}}), z_f \rangle &= 0, \\ -\langle \kappa_b \nabla \theta_b, \nabla z_b \rangle - \langle h_{\text{air}}(\theta_b - \theta_{\text{amb}}), z_b \rangle &= 0, \\ -\langle (\lambda + \frac{1 - 2\phi_f}{D})(\nabla \cdot \mathbf{u}_s) \mathbf{I} + \mu(\nabla \mathbf{u}_s + (\nabla \mathbf{u}_s)^T), \mathbf{w}_u \rangle + \langle \mathbf{t}, \mathbf{w}_u \rangle &= 0, \\ -\langle (\lambda_b)(\nabla \cdot \mathbf{u}_b) \mathbf{I} + \mu_b(\nabla \mathbf{u}_b + (\nabla \mathbf{u}_b)^T), \mathbf{w}_b \rangle + \langle \mathbf{t}, \mathbf{w}_b \rangle &= 0, \end{aligned}$$

for all test functions $\mathbf{v} = (z_s, z_f, z_b, \mathbf{w}_u, \mathbf{w}_b) \in \mathcal{V}$. Here \mathcal{U} and \mathcal{V} are Hilbert spaces, and $\langle \cdot, \cdot \rangle$ represents the inner product on the corresponding function spaces. The weak form (7) is then represented as,

$$r(\mathbf{u}, \mathbf{v}, m, d) := \nu \langle \mathbf{v}, \mathcal{R}(\mathbf{u}, m, d) \rangle_{\mathcal{V}'} = 0 \quad \forall \mathbf{v} \in \mathcal{V} \quad (7)$$

where $\nu \langle \cdot, \cdot \rangle_{\mathcal{V}'}$ represent the duality pairing between the \mathcal{V} and \mathcal{V}' .

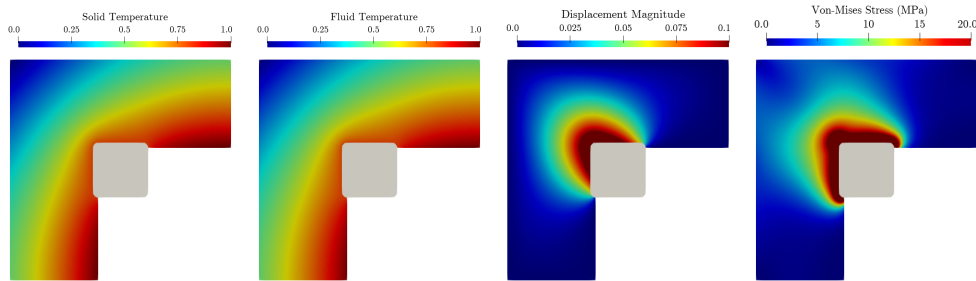


Figure 2: Finite element solution of the forward model for the beam-insulator system with constant porosity $\phi_f = 0.7$, depicting the solid temperature θ_s , fluid temperature θ_f , displacement magnitude $\|\mathbf{u}_s\|$, and von Mises stress T_{VM} .

Figure 2 presents the deterministic finite element solution of the forward model for the beam-insulator system under constant porosity $\phi_f = 0.7$, utilizing the model parameters listed in Table 1. Thermal expansion of the thermoelastic concrete beam induces stress concentrations within the aerogel

thermal break, risking mechanical failure. This can be mitigated by varying the aerogel’s porosity across the insulation, maintaining its effectiveness in interrupting heat transfer between the building interior and exterior.

Design objectives. The design objective Q is defined as thermal compliance of the aerogel thermal break component over domain Ω ,

$$Q = \frac{1}{2} \sum_{i=s,f} \langle \phi_i \kappa_i \nabla \theta_i, \nabla \theta_i \rangle + \langle \phi_i h_{\text{air}}(\theta_i - \theta_{\text{amb}}), \theta_i \rangle, \quad (8)$$

The design problem focuses on determining the spatial distribution of the fluid volume fraction (porosity), $\phi_f(\mathbf{x})$, to minimize stress concentrations within the thermal break, thereby preventing mechanical failure while preserving its thermal insulation performance.

2.2. Uncertain design parameter

Due to the inherent challenges in precisely controlling the properties of additively manufactured aerogel, considerable uncertainty arises in the porosity values within the thermal break. To effectively model uncertainty, a design parameter as a spatial field $d \in [0, 1]$ is introduced, employing a sigmoid mapping function, ensuring that porosity values asymptotically remain within the physically valid range, maintaining near-linear behavior within $\phi_f \in [90\%, 10\%]$, and minimize the impact on the spatial correlation length, such that [31]

$$\phi_f \equiv \text{sigmoid}(d + m). \quad (9)$$

The uncertain parameter m is represented as a Gaussian random field characterized by the Matérn covariance kernel. Specifically, m is distributed as $\mathcal{N}(\bar{m}, \mathcal{C})$ where \bar{m} is the mean and \mathcal{C} is the covariance operator. The sampling of Gaussian random field m is equivalent to solving the elliptic equation with a robin boundary condition,

$$\begin{aligned} -\gamma \nabla \cdot (\Theta \nabla m) + \delta m &= \dot{W} \quad \text{in } \Omega \\ m + 1.42 \nabla m \cdot \mathbf{n} &= 0 \quad \text{on } \Gamma \end{aligned} \quad (10)$$

where ∇ is gradient operator, Δ is the Laplace operator and \mathbf{n} is the outward unit normal vector. Here, W represents the spatial White Gaussian noise with a unit variance, and the parameters γ and δ control the variance $\sigma^2 =$

$1/4\pi\delta\gamma$ and spatial correlation length $L_c = \sqrt{8\gamma/\delta}$. The factor $\sqrt{\delta\gamma}/1.42$ (Robin coefficient) is chosen to minimize boundary artifacts [46], and Θ is a symmetric positive definite two-dimensional (2D) anisotropic tensor

$$\Theta = \begin{bmatrix} \vartheta_x \sin^2(\alpha) + \vartheta_y \cos^2(\alpha) & (\vartheta_x - \vartheta_y) \sin(\alpha) \cos(\alpha) \\ (\vartheta_x - \vartheta_y) \sin(\alpha) \cos(\alpha) & \vartheta_x \cos^2(\alpha) + \vartheta_y \sin^2(\alpha) \end{bmatrix} \quad (11)$$

where α is the angle between the magnitudes ϑ_x and ϑ_y in x and y directions, respectively.

2.3. Chance-constrained PDE-constrained optimal design under uncertainty

We consider the design problem as minimizing the design objective, thermal compliance in (8), while accounting for uncertainty in objective through its explicit dependence on the uncertain parameter m , i.e., $Q(d, m)$. Extending the mean-variance optimization, e.g., [18, 19, 31], the cost functional for the proposed optimal design takes the form,

$$\mathcal{J}(d) = \mathbb{E}[Q(d, m)] + \beta_V \mathbb{V}[Q(d, m)] + \beta_R R(d). \quad (12)$$

To prevent mechanical failure of the aerogel thermal break due to stress concentration, the maximum von Mises stress T_{VM} must remain below a critical threshold. This requirement is incorporated as a probabilistic (chance) constraint in the optimization problem, as T_{VM} depends on uncertain parameters. However, due to the non-differentiable nature of the maximum stress, direct optimization poses significant challenges. This challenge is addressed using stress aggregation function based on p-norm [41], which is a smooth approximation of the maximum stress and enables gradient-based optimization techniques. The p-norm for the von Mises stress can be computed as

$$T_{pn} = \left(\int_{\Omega} T_{VM}^p d\Omega \right)^{\frac{1}{p}} \quad (13)$$

The chance constraint function can hence be written as,

$$f = T_{cr} - T_{pn}, \quad (14)$$

where T_{cr} is the limiting critical stress and T_{pn} is the p-norm of the von Mises stress over the domain. To avoid stress concentration, we consider a chance

constraint:

$$P(f(m, d) \geq 0) \leq \alpha_c, \quad (15)$$

for a critical chance $0 < \alpha_c < 1$. The probability is given by

$$\begin{aligned} P(f(m, d) \geq 0) &= \mathbb{E}[\mathbb{I}_{[0, \infty]}(f(m, d))] \\ &= \int_{\mathcal{M}} \mathbb{I}_{[0, \infty]}(f(m, d)) d\mu(m), \end{aligned} \quad (16)$$

where $\mathbb{I}_{[0, \infty]}(f(m, d))$ is an indicator function defined as:

$$\mathbb{I}_{[0, \infty]}(f(m, d)) = \begin{cases} 1 & \text{if } f(m, d) \geq 0 \\ 0 & \text{if } f(m, d) < 0 \end{cases} \quad (17)$$

uncertainty as,

$$\begin{aligned} d_{\text{opt}}(\mathbf{x}) &= \min_d \mathcal{J}(d) \\ &\text{s.t. } \mathcal{R}(\mathbf{u}, m, d) = 0 \\ &\quad P(f(m, d) \geq 0) \leq \alpha_c \quad \text{in } \Omega \end{aligned} \quad (18)$$

Monte Carlo estimation. A common approach to compute the mean and variance terms in (12) is the Monte Carlo estimation for N_{mc} samples,

$$\mathbb{E}[Q] \approx \frac{1}{N_{mc}} \sum_{i=1}^{N_{mc}} Q(m^{(i)}), \quad (19)$$

$$\mathbb{V}[Q] \approx \left(\frac{1}{N_{mc}} \sum_{i=1}^{N_{mc}} Q^2(m^{(i)}) \right) - \left(\frac{1}{N_{mc}} \sum_{i=1}^{N_{mc}} Q(m^{(i)}) \right)^2, \quad (20)$$

where $\{m^{(i)}\}_{i=1}^{N_{mc}}$ are independent and identically distributed (i.i.d) random samples from the uncertain and spatially correlated parameter. Similarly, the chance constraint function can be approximated by

$$P(f(\cdot, d) \geq 0) := \frac{1}{M_f} \sum_{i=1}^{M_f} \mathbb{I}_{[0, \infty]}(f(m_i, d)) \quad (21)$$

To achieve an accurate approximation, particularly for f_M for α close to 0, a large number of samples are required due to slow convergence of the Monte

Carlo method. The convergence rate of Monte Carlo method is $\mathcal{O}(\frac{1}{\sqrt{N_{mc}}})$, therefore for accurate computation of the cost functional (12), a considerable number of PDE model evaluations will be required, making the optimization under uncertainty problem computationally prohibitive.

3. Scalable framework for chance constrained optimal design

In this section, we present a computationally tractable approach by approximating the mean and variance of the design objective by means of low-order Taylor expansion [18, 19]. The quadratic Taylor approximation of Q at the mean of the uncertain parameter \bar{m} , assuming Q is sufficiently smooth and Fréchet differentiable with respect to uncertain parameter is derived as,

$$\begin{aligned} Q_{\text{QUAD}}(m) &= \sum_{l=0}^2 \partial_m^l Q(\bar{m}) (m - \bar{m})^l \\ &= \bar{Q} + \langle \bar{Q}^m, m - \bar{m} \rangle + \frac{1}{2} \langle \bar{Q}^{mm} (m - \bar{m}), m - \bar{m} \rangle. \end{aligned} \quad (22)$$

where $\partial_m^l Q(\bar{m})$ is the l -th order tensor derivative at \bar{m} and the objective Q and its gradient and Hessian with respect to m , evaluated at mean \bar{m} , denoted as \bar{Q} , \bar{Q}^m and \bar{Q}^{mm} , respectively. The close form for the expectation of the quadratic Taylor approximation in (22), considering $\mathbb{E}[\bar{Q}] = \bar{Q}$ and $\mathbb{E}[\langle \bar{Q}^m, m - \bar{m} \rangle] = 0$, and Lemma 1 of [47], is obtained as

$$\mathbb{E}[Q_{\text{QUAD}}] = \bar{Q} + \frac{1}{2} \text{tr}(\bar{\mathcal{H}}_c), \quad (23)$$

where $\bar{\mathcal{H}}_c = \mathcal{C} \bar{Q}^{mm}$ denotes the covariance preconditioned Hessian computed at the mean of m and $\text{tr}(\cdot)$ is trace operator. Moreover, noting that variance is invariant with respect to its deterministic translation, e.g., $\mathbb{V}(m - \text{const.}) = \mathbb{V}(m)$, one can write,

$$\mathbb{E}[(Q_{\text{QUAD}}(m) - \bar{Q})^2] = \mathbb{E}[(\langle \bar{Q}^m, m - \bar{m} \rangle + \frac{1}{2} \langle \bar{Q}^{mm} (m - \bar{m}), m - \bar{m} \rangle)^2], \quad (24)$$

which, upon expansion, allows each term to be expressed as

$$\begin{aligned}\mathbb{E}[(\langle \bar{Q}^m, m - \bar{m} \rangle)^2] &= \langle \bar{Q}^m, \mathcal{C} \bar{Q}^m \rangle, \\ \mathbb{E}[(\langle \bar{Q}^{mm}(m - \bar{m}), m - \bar{m} \rangle)^2] &= \text{tr}(\bar{\mathcal{H}}_c)^2 + 2 \text{tr}((\bar{\mathcal{H}}_c)^2), \\ \mathbb{E}[\langle \bar{Q}^m, m - \bar{m} \rangle \langle \bar{Q}^{mm}(m - \bar{m}), m - \bar{m} \rangle] &= 0.\end{aligned}\quad (25)$$

Furthermore, the square of the first moment of $Q_{\text{QUAD}}(m) - \bar{Q}$ can be written as,

$$(\mathbb{E}[Q_{\text{QUAD}}(m) - \bar{Q}])^2 = (\mathbb{E}[Q_{\text{QUAD}}(m)] - \mathbb{E}[\bar{Q}])^2 = \frac{1}{4}(\text{tr}(\bar{\mathcal{H}}_c))^2 \quad (26)$$

From (25) and (26), the variance of the quadratic Taylor approximation of Q in (22) is obtained as,

$$\mathbb{V}[Q_{\text{QUAD}}(m)] = \mathbb{V}[Q_{\text{QUAD}}(m) - \bar{Q}] = \langle \bar{Q}^m, \mathcal{C} \bar{Q}^m \rangle + \frac{1}{2} \text{tr}((\bar{\mathcal{H}}_c)^2). \quad (27)$$

Consequently, the mean and variance of the design objective in (12) can be replaced by their corresponding quadratic Taylor approximations in (23) and (27), respectively, leading to the approximated design objective as

$$\mathcal{J}_{\text{QUAD}}(d) = \bar{Q} + \frac{1}{2} \text{tr}(\bar{\mathcal{H}}_c) + \beta_V \left(\langle \bar{Q}^m, \mathcal{C} \bar{Q}^m \rangle + \frac{1}{2} \text{tr}((\bar{\mathcal{H}}_c)^2) \right) + \beta_R R(d). \quad (28)$$

Similar to (22), we can construct a second-order Taylor expansion of the constraint function f at \bar{m} as,

$$f_{\text{QUAD}}(m) = \bar{f} + \langle \bar{f}^m, m - \bar{m} \rangle + \frac{1}{2} \langle \bar{f}^{mm}(m - \bar{m}), m - \bar{m} \rangle. \quad (29)$$

The probability $P(f(\cdot, d) \geq 0)$ by Monte Carlo estimator (21) with the quadratic approximation yields,

$$P(f(m, d) \geq 0) = \frac{1}{M_f} \mathbb{I}_{[0, \infty)}(f_{\text{QUAD}}(m_i, d)). \quad (30)$$

This approximation of the constraint function obviates the necessity for a large number of PDE solves to assess the probability utilizing sample averaging methods. In upcoming sections, we present the Lagrangian formalism to derive the m -gradient and m -Hessian, representing the gradient and Hessian

of Q with respect to m . We also introduce an efficient method for evaluating the covariance preconditioned Hessian, $\bar{\mathcal{H}}_c$.

3.1. Analytical gradient and hessian of design objective with respect to the uncertain parameter

The Lagrangian functional, considering the adjoint variable \mathbf{v}^Q as the Lagrange multiplier associated with the state equation with respect to the objective function Q , is defined as,

$$\mathcal{L}(\mathbf{u}, \mathbf{v}^Q, m, d) = Q(\mathbf{u}, m, d) + r(\mathbf{u}, \mathbf{v}^Q, m, d), \quad (31)$$

where $r(\mathbf{u}, \mathbf{v}, m, d)$ is the weak form in (7). By imposing the condition that the first-order variation of the Lagrangian functional at \bar{m} with respect to the adjoint variable \mathbf{v} and the state variable \mathbf{u} is equal to zero, we obtain, the state problem:

$$\text{Find } \mathbf{u} \in \mathcal{U}, \text{ such that } \langle \tilde{\mathbf{v}}, \partial_{\mathbf{v}} \bar{r} \rangle = 0, \quad \forall \tilde{\mathbf{v}} \in \mathcal{V}, \quad (32)$$

and adjoint problem:

$$\text{Find } \mathbf{v} \in \mathcal{V}, \text{ such that } \langle \tilde{\mathbf{u}}, \partial_{\mathbf{u}} \bar{r}^Q \rangle = -\langle \tilde{\mathbf{u}}, \partial_{\mathbf{u}} \bar{Q} \rangle, \quad \forall \tilde{\mathbf{u}} \in \mathcal{U}. \quad (33)$$

In the above relations, $(\bar{\cdot})$ denotes the quantities computed at the mean of the uncertain parameter, and $(\tilde{\cdot})$ indicates directional variables. Directional variables are referred to the variables that define the direction along which perturbation is considered to compute the change in the functional to obtain the derivative of the functional. Also, here we define $r^Q = r(\mathbf{u}, \mathbf{v}^Q, m, d)$ for ease of notation. The gradient of Q at \bar{m} acting in the direction $\tilde{m} = m - \bar{m}$ is then given by,

$$\langle \tilde{m}, \bar{Q}^m \rangle = \langle \tilde{m}, \partial_m \mathcal{L} \rangle = \langle \tilde{m}, \partial_m \bar{Q} + \partial_m \bar{r}^Q \rangle \quad \forall \tilde{m} \in \mathcal{M} \quad (34)$$

Thus, evaluating m -gradient in (34) requires the solution of state problem (32) for \mathbf{u} and the adjoint problem (33) for \mathbf{v} .

To solve for the m -Hessian, consider a meta-Lagrangian functional with incremental state $\hat{\mathbf{u}}$ and adjoint $\hat{\mathbf{v}}$

$$\mathcal{L}^H(\mathbf{u}, \mathbf{v}^Q, m, d; \hat{\mathbf{u}}^Q, \hat{\mathbf{v}}^Q, \hat{m}^Q) = \langle \hat{m}^Q, \partial_m \bar{r}^Q + \partial_m \bar{Q} \rangle + \langle \hat{\mathbf{v}}^Q, \partial_{\mathbf{v}} \bar{r}^Q \rangle + \langle \hat{\mathbf{u}}^Q, \partial_{\mathbf{u}} \bar{r}^Q + \partial_{\mathbf{u}} \bar{Q} \rangle \quad (35)$$

where the terms on the right-hand side are m -gradient, forward, and adjoint problems, respectively. Repeating the similar process of vanishing the first variation of the Lagrangian functional with respect to adjoint and state, we obtain the incremental state problem:

$$\text{Find } \hat{\mathbf{u}} \in \mathcal{U}, \text{ such that } \langle \tilde{\mathbf{v}}, \partial_{\mathbf{v}\mathbf{u}} \bar{r}^Q \hat{\mathbf{u}}^Q \rangle = -\langle \tilde{\mathbf{v}}, \partial_{\mathbf{v}m} \bar{r}^Q \hat{m}^Q \rangle, \quad \forall \tilde{\mathbf{v}} \in \mathcal{V}, \quad (36)$$

and the incremental adjoint problem:

$$\text{Find } \hat{\mathbf{v}} \in \mathcal{V}, \text{ such that}$$

$$\langle \tilde{\mathbf{u}}, \partial_{\mathbf{u}\mathbf{v}} \bar{r}^Q \hat{\mathbf{v}}^Q \rangle = -\langle \tilde{\mathbf{u}}, \partial_{\mathbf{u}\mathbf{u}} \bar{r}^Q \hat{\mathbf{u}} + \partial_{\mathbf{u}\mathbf{u}} \bar{Q} \hat{\mathbf{u}}^Q + \partial_{\mathbf{u}m} \bar{r}^Q \hat{m}^Q + \partial_{\mathbf{u}m} \bar{Q} \hat{m}^Q \rangle, \quad \forall \tilde{\mathbf{u}} \in \mathcal{U}. \quad (37)$$

By taking the variation of \mathcal{L}^H with respect to m as zero, the Hessian $Q_{mm}(\bar{m})$ acting on \hat{m} is computed as,

$$\begin{aligned} \langle \tilde{m}, \bar{Q}^{mm} \hat{m}^Q \rangle = & \langle \tilde{m}, \partial_{m\mathbf{v}} \bar{r}^Q \hat{\mathbf{v}}^Q + \partial_{m\mathbf{u}} \bar{r}^Q \hat{\mathbf{u}}^Q + \partial_{m\mathbf{u}} \bar{Q} \hat{\mathbf{u}}^Q + \partial_{mm} \bar{r}^Q \hat{m}^Q \\ & + \partial_{mm} \bar{Q} \hat{m}^Q \rangle \end{aligned} \quad (38)$$

We remark that the last term on the right-hand side of (37) and the last two terms on the right-hand side of (38) are included due to the explicit dependence of the design objective (8) on the uncertain parameter in our problem. Thus, evaluating the m -Hessian acting on \hat{m} in (38) requires the solution of the incremental state problem (36) for $\hat{\mathbf{u}}$ and the incremental adjoint problem (37) for $\hat{\mathbf{v}}$.

Similarly, we can compute the gradient and Hessian action of f . The adjoint problem can be written as:

$$\langle \tilde{\mathbf{u}}, \partial_{\mathbf{u}} \bar{r}^f \rangle = -\langle \tilde{\mathbf{u}}, \partial_{\mathbf{u}} \bar{f} \rangle, \quad \forall \tilde{\mathbf{u}} \in \mathcal{U} \quad (39)$$

The gradient of f at \bar{m} can be defined as:

$$\langle \tilde{m}, \bar{f}^m \rangle = \langle \tilde{m}, \partial_m \bar{f} + \partial_m \bar{r}^f \rangle \quad \forall \tilde{m} \in \mathcal{M} \quad (40)$$

Then by solving incremental state problem,

$$\begin{aligned} & \text{Find } \hat{\mathbf{u}}^f \in \mathcal{U}, \text{ such that} \\ \langle \tilde{\mathbf{v}}, \partial_{\mathbf{v}\mathbf{u}} \bar{r}^f \hat{\mathbf{u}}^f \rangle = & -\langle \tilde{\mathbf{v}}, \partial_{\mathbf{v}m} \bar{r}^f \hat{m}^f \rangle \quad \forall \tilde{\mathbf{v}} \in \mathcal{V} \end{aligned} \quad (41)$$

and the incremental adjoint problem

$$\begin{aligned}
& \text{Find } \hat{\mathbf{v}}^f \in \mathcal{U}, \text{ such that} \\
\langle \tilde{\mathbf{u}}, \partial_{\mathbf{u}\mathbf{v}} \bar{r}^f \hat{\mathbf{v}}^f \rangle &= -\langle \tilde{\mathbf{u}}, \partial_{\mathbf{u}\mathbf{u}} \bar{r}^f \hat{\mathbf{u}}^f + \partial_{\mathbf{u}\mathbf{u}} \bar{f} \hat{\mathbf{u}}^f + \partial_{\mathbf{u}m} \bar{r}^f \hat{m}^f + \partial_{\mathbf{u}m} \bar{f} \hat{m}^f \rangle \quad \forall \tilde{\mathbf{u}} \in \mathcal{U}
\end{aligned} \tag{42}$$

We obtain the Hessian action of f at \tilde{m}

$$\begin{aligned}
\langle \tilde{m}, \bar{f}^{mm} \hat{m}^f \rangle &= \langle \tilde{m}, \partial_{m\mathbf{v}} \bar{r}^f \hat{\mathbf{v}}^f + \partial_{m\mathbf{u}} \bar{r}^f \hat{\mathbf{u}}^f + \partial_{m\mathbf{u}} \bar{f} \hat{\mathbf{u}}^f + \partial_{mm} \bar{r}^f \hat{m}^f + \partial_{mm} \bar{f} \hat{m}^f \rangle \\
&\quad \forall \tilde{m} \in \mathcal{M}
\end{aligned} \tag{43}$$

3.2. Monte Carlo with control variate

The approximation of $\mathbb{E}[Q]$ and $\mathbb{V}[Q]$ in the cost functional (12) using a quadratic Taylor series expansion may lack accuracy for the design problem, particularly for design problems where the variance of the uncertain parameter m is large, as shown in [31]. To enhance accuracy, the quadratic approximation Q_{QUAD} is leveraged as a control variate to reduce variance in the Monte Carlo estimators for the mean and variance. This involves correcting the moments of Q_{QUAD} by applying a Monte Carlo method to estimate the mean and variance of the residual between Q and its quadratic approximation Q_{QUAD} . We can use the same $M = M_1 = M_2$ random samples for the approximation of the mean and variance. For mean of control variate approximation

$$\begin{aligned}
\mathbb{E}[Q_{CV}] &\approx \mathbb{E}[Q] = \mathbb{E}[Q_{\text{QUAD}}] + \mathbb{E}[Q - Q_{\text{QUAD}}] := Q(\bar{m}) + \frac{1}{2} \text{tr}(\mathcal{H}) \\
&+ \frac{1}{M} \sum_{i=1}^M \left(Q(m_i) - Q(\bar{m}) - \langle m_i - \bar{m}, Q^m(\bar{m}) \rangle - \frac{1}{2} \langle m_i - \bar{m}, Q^{mm}(\bar{m})(m_i - \bar{m}) \rangle \right).
\end{aligned} \tag{44}$$

The variance can be written as

$$\begin{aligned}
\mathbb{V}[Q_{CV}] &= \mathbb{E}[(Q_{\text{QUAD}} - Q(\bar{m}))^2] + \mathbb{E}[(Q - Q(\bar{m}))^2 - (Q_{\text{QUAD}} - Q(\bar{m}))^2] \\
&\quad - (\mathbb{E}[Q_{\text{QUAD}} - Q(\bar{m})] + \mathbb{E}[(Q - Q(\bar{m})) - (Q_{\text{QUAD}} - Q(\bar{m}))])^2,
\end{aligned} \tag{45}$$

which can be approximated by

$$\begin{aligned}
\mathbb{V}[Q_{CV}] &:= \langle \mathcal{C}Q^m(\bar{m}), Q^m(\bar{m}) \rangle + \frac{1}{4}(\text{tr}(\mathcal{H}))^2 + \frac{1}{2}\text{tr}(\mathcal{H}^2) \\
&+ \frac{1}{M} \sum_{i=1}^M \left((Q(m_i) - Q(\bar{m}))^2 - \left(\langle m_i - \bar{m}, Q^m(\bar{m}) \rangle + \frac{1}{2} \langle m_i - \bar{m}, Q^{mm}(\bar{m})(m_i - \bar{m}) \rangle \right)^2 \right) \\
&- \left(\frac{1}{2}\text{tr}(\mathcal{H}) + \frac{1}{M} \sum_{i=1}^M \left(Q(m_i) - \langle m_i - \bar{m}, Q^m(\bar{m}) \rangle - \frac{1}{2} \langle m_i - \bar{m}, Q^{mm}(\bar{m})(m_i - \bar{m}) \rangle \right) \right)^2.
\end{aligned} \tag{46}$$

The number of samples M required to achieve the desired accuracy (and hence the computational cost) depends on the variance of the integrand and how closely the quadratic approximation matches the high-fidelity Monte Carlo estimation. A closer approximation reduces the required M , while a poorer match increases it. Notably, if the quadratic approximation is highly correlated with Q , fewer Monte Carlo samples are needed for effective variance reduction and accurate approximation.

3.3. Randomized trace estimator

The equations for the mean (23) and variance (27) of the design objectives evaluated using the quadratic approximation requires the trace of the covariance-preconditioned Hessian $\bar{\mathcal{H}}_c$, which typically comes out to be a large dense matrix. The traditional approach is based on Monte Carlo method, where the Hessian action is computed on a certain number of randomly chosen directions from a Gaussian distribution [18].

Despite adhering to the lower bounds on the required number of samples for accurate trace approximations, as outlined in [48], a large number of samples is still necessary. Given the large sample size needed at each optimization iteration, this approach becomes computationally prohibitive for the design under uncertainty problem addressed in this work. Here, we implement a randomized approximated eigen-decomposition for computing the trace and trace-squared using the dominant eigenvalues $\{\lambda_n\}_{n=1}^{N_{\text{eig}}}$ of the covariance-preconditioned Hessian $\bar{\mathcal{H}}_c$, expressed as,

$$\text{tr}(\bar{\mathcal{H}}_c) \approx \sum_{n \geq 1}^{N_{\text{eig}}} \lambda_n, \quad \text{tr}(\bar{\mathcal{H}}_c^2) \approx \sum_{n \geq 1}^{N_{\text{eig}}} \lambda_n^2. \tag{47}$$

The above forms of trace estimators are justified by the symmetric positive definite property of the operator $\bar{\mathcal{H}}_c$. It is important to note that the value of

N_{eig} does not depend on the actual parameter dimension, but is dependent on the effective dimension of the parameter, e.g., [49, 50, 51, 52] it tends to be small when the covariance-preconditioned Hessian is low-rank or when its eigenvalues decay rapidly (see the numerical results of Section 5).

The eigenvalues λ_n are obtained by solving the following generalized eigenvalue problem,

$$\langle \zeta, \bar{Q}^{mm} \psi_j \rangle = \lambda_j \langle \zeta, \mathcal{C}^{-1} \psi_j \rangle, \quad \forall \zeta \in \mathcal{M}, \quad j = 1, \dots, N_{\text{eig}} \quad (48)$$

where the eigenvectors ψ_j exhibit orthonormality with \mathcal{C}^{-1} , $\langle \psi_i, \mathcal{C}^{-1} \psi_j \rangle = \delta_{ij}$, $i, j = 1, \dots, N_{\text{eig}}$ and δ_{ij} denotes the Kronecker delta function. Using an n -degree finite element discretization, (48) is rewritten in the form of matrix as $\mathbf{M} \boldsymbol{\psi} = \lambda \mathbf{K} \boldsymbol{\psi}$ where \mathbf{M}, \mathbf{K} are n -by- n symmetric matrices, and \mathbf{K} is positive definite, $\boldsymbol{\psi}$ represents a vector of size n . For solving the resulting eigenproblem, we implement a randomized algorithm [53], discussed in Algorithm 1.

Algorithm 1: Double-Pass Randomized Eigenvalue Solver

Input : Matrices $\mathbf{M}, \mathbf{K} \in \mathbb{R}^{n \times n}$ obtained from finite element discretization, number of eigenpairs requested N_{eig} , oversampling parameter N_p

Output: Eigenpairs (λ_j, ψ_j) for $j = 1, \dots, N_{\text{eig}}$

- 1 Generate random sample and draw a Gaussian random matrix $\boldsymbol{\Omega} \in \mathbb{R}^{n \times (N_{\text{eig}} + N_p)}$;
- 2 Form the range matrix $\mathbf{Z} = \mathbf{K}^{-1}(\mathbf{M}\boldsymbol{\Omega})$;
- 3 Perform QR factorization $\mathbf{Z} = \mathbf{Q}\mathbf{R}$ such that $\mathbf{Q}^\top \mathbf{M}\mathbf{Q} = \mathbf{I}_{N_{\text{eig}} + N_p}$;
- 4 Compute the reduced matrix $\mathbf{Q}^\top \mathbf{K}\mathbf{Q}$;
- 5 Compute the eigendecomposition $\mathbf{U}\boldsymbol{\Lambda}\mathbf{U}^\top$, where $\boldsymbol{\Lambda} = \text{diag}(\lambda_1, \lambda_2, \dots)$;
- 6 Obtain the eigenpairs of the original problem:

$$\lambda_j = \boldsymbol{\lambda}[j, j], \quad \psi_j = \mathbf{Q}\mathbf{U}[:, j], \quad j = 1, \dots, N_{\text{eig}}.$$

4. Gradient-based optimization

To solve the optimization problem (18), we employ the Inexact Newton Conjugate-Gradient optimization algorithm (INCG), leveraging an approxi-

mate Newton approach combined with a backtracking line search to ensure global convergence [20, 54]. In this method, the Hessian is approximated by evaluating it at the mean of the random field, while the gradient is computed precisely. The resulting Newton system is then solved approximately using a preconditioned conjugate gradient method in a matrix-free manner, allowing for efficient computation. However, applying INCG to solve (18) in a scalable manner requires special treatment of the chance constraints and efficient computation of the gradient of the cost functional with respect to high-dimensional design parameters, as discussed in this section.

4.1. Smooth approximation of the discontinuous function

The indicator function utilized in the chance constraint exhibits discontinuity at $f(m, d) = 0$. To employ the gradient-based INCG, this discontinuous indicator function must be approximated with a smooth, continuous counterpart. One approach involves employing a logistic function as a smooth approximation of the indicator function [25] such that,

$$\mathbb{I}_{[0, \infty]}(x) \approx l_\omega(x) = \frac{1}{1 + e^{-2\omega x}}, \quad (49)$$

where a larger ω corresponds to a sharper transition at $x = 0$ as shown in Figure 3. This smooth approximation tackles the non-differentiability of the chance constraint and makes the cost functional differentiable with respect to the design variable.

4.2. Penalty Method

To impose the inequality constraint (15), a quadratic penalty method [55] is applied. The quadratic penalty function is defined as,

$$S_\gamma(x) = \frac{\gamma}{2}(\max\{0, x\})^2 \quad (50)$$

where $\gamma > 0$ is a constant corresponding to the weight of the penalty. Using the penalty method, the chance-constrained problem can be rewritten as

$$\min_{d \in [0, 1]} \mathcal{J}(d) + \mathcal{S}_\gamma(\mathbb{E}[l_\omega(f)] - \alpha_c) \quad (51)$$

This transformation simplifies the inequality-constrained problem by converting it into an unconstrained form.

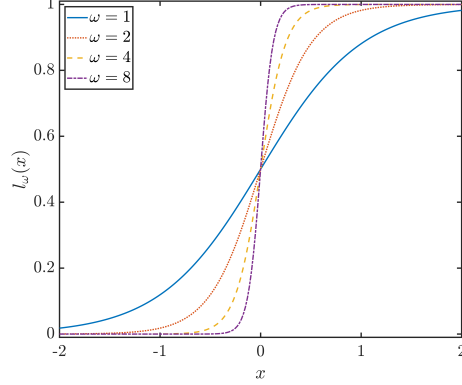


Figure 3: Approximation of the discontinuous indicator function $\mathbb{I}_{[0, \infty]}(x)$ with a smooth logistic function as given in (49) and its convergence with increasing ω

4.3. Design gradients via adjoint

The Lagrangian formalism is employed to derive the gradient of the quadratic approximation of the design objective $\mathcal{J}_{\text{QUAD}}(d)$ with respect to the design parameter, referred to as the d-gradient. This gradient provides critical information to the INCG optimizer, in order to facilitate gradient-based optimization processes. By substituting the trace estimators (47) into (28) and converting it into unconstrained problem using quadratic penalty (50) and smooth approximation (49), we have

$$\begin{aligned} \mathcal{J}_{\text{QUAD}}(d) = & \left(\bar{Q} + \frac{1}{2} \sum_{j \geq 1}^{N_{\text{eig}}} \lambda_j^Q \right) + \beta_V \left(\langle \bar{Q}^m, \mathcal{C} \bar{Q}^m \rangle + \frac{1}{2} \sum_{j \geq 1}^{N_{\text{eig}}} (\lambda_j^Q)^2 \right) + \beta_R R(d) \\ & + S_{\gamma}(\mathbb{E}[l_{\omega}(f_{\text{QUAD}}(m, d))] - \alpha_c) \end{aligned} \quad (52)$$

To evaluate the d -gradient, we consider a quadratic meta-Lagrangian functional

$$\begin{aligned}
\mathcal{L}_{\text{QUAD}}(d, \mathbf{u}, \mathbf{v}^*, \{\lambda_j^Q\}, \{\psi_j^Q\}, \{\hat{\mathbf{u}}_j^Q\}, \{\hat{\mathbf{v}}_j^Q\}, \\
(\mathbf{u}^Q)^*, (\mathbf{v}^Q)^*, \{(\lambda_j^Q)^*\}, \{(\psi_j^Q)^*\}, \{(\hat{\mathbf{u}}_j^Q)^*\}, \{(\hat{\mathbf{v}}_j^Q)^*\}, \\
\{\lambda_j^f\}, \{\psi_j^f\}, \{\hat{\mathbf{u}}_j^f\}, \{\hat{\mathbf{v}}_j^f\}, (\mathbf{u}^f)^*, (\mathbf{v}^f)^*, \{(\lambda_j^f)^*\}, \{(\psi_j^f)^*\}, \{(\hat{\mathbf{u}}_j^f)^*\}, \{(\hat{\mathbf{v}}_j^f)^*\}) \\
= \mathcal{J}_{\text{QUAD}}(d) + \langle \mathbf{v}^*, \partial_{\mathbf{v}} \bar{r}^Q \rangle \\
+ \langle (\mathbf{u}^Q)^*, \partial_{\mathbf{u}} \bar{r}^Q + \partial_{\mathbf{u}} \bar{Q} \rangle \\
+ \sum_{j=1}^{N_{\text{eig}}^Q} \langle (\psi_j^Q)^*, (\bar{Q}^{mm} - \lambda_j^Q \mathcal{C}^{-1}) \psi_j^Q \rangle \\
+ \sum_{j=1}^{N_{\text{eig}}^Q} \left((\lambda_j^Q)^* (\langle \psi_j^Q, \mathcal{C}^{-1} \psi_j^Q \rangle - 1) + \sum_{j=1}^{N_{\text{eig}}^Q} \langle \hat{\mathbf{v}}_j^{Q*}, \partial_{\mathbf{v}\mathbf{u}} \bar{r}_Q \hat{\mathbf{u}}_j^Q + \partial_{\mathbf{v}m} \bar{r}_Q \psi_j^Q \rangle \right) \\
+ \sum_{j=1}^{N_{\text{eig}}^Q} \langle (\hat{\mathbf{u}}_j^Q)^*, \partial_{\mathbf{u}\mathbf{v}} \bar{r}_Q \hat{\mathbf{v}}_j^Q + \partial_{\mathbf{u}\mathbf{u}} \bar{r}_Q (\mathbf{u}^Q)^* + \partial_{\mathbf{u}\mathbf{u}} \bar{Q} \hat{\mathbf{u}}_j^Q + \partial_{\mathbf{u}m} \bar{Q} \psi_j^Q + \partial_{\mathbf{u}m} \bar{r}_Q \psi_j^Q \rangle \\
+ \langle (\mathbf{u}^f)^*, \partial_{\mathbf{u}} \bar{r}_f + \partial_{\mathbf{u}} \bar{f} \rangle \\
+ \sum_{j=1}^{N_{\text{eig}}^f} \langle (\psi_j^f)^*, (\bar{f}^{mm} - \lambda_j^f \mathcal{C}^{-1}) \psi_j^f \rangle \\
+ \sum_{j=1}^{N_{\text{eig}}^f} \left((\lambda_j^f)^* (\langle \psi_j^f, \mathcal{C}^{-1} \psi_j^f \rangle - 1) + \sum_{j=1}^{N_{\text{eig}}^f} \langle (\hat{\mathbf{v}}_j^f)^*, \partial_{\mathbf{v}\mathbf{u}} \bar{r}_f \hat{\mathbf{u}}_j^f + \partial_{\mathbf{v}m} \bar{r}_f \psi_j^f \rangle \right) \\
+ \sum_{j=1}^{N_{\text{eig}}^f} \langle (\hat{\mathbf{u}}_j^f)^*, \partial_{\mathbf{u}\mathbf{v}} \bar{r}_f \hat{\mathbf{v}}_j^f + \partial_{\mathbf{u}\mathbf{u}} \bar{r}_f (\mathbf{u}^f)^* + \partial_{\mathbf{u}\mathbf{u}} \bar{f} \hat{\mathbf{u}}_j^f + \partial_{\mathbf{u}m} \bar{f} \psi_j^f + \partial_{\mathbf{u}m} \bar{r}_f \psi_j^f \rangle
\end{aligned} \tag{53}$$

where $(\cdot)^*$ represents the adjoint variables, $(\dot{\cdot})$ denotes the incremental variables. The terms on the right hand side of (53), correspond to the following: the quadratic approximation of the design objective (28), the state (32) and adjoint (33) problems for design objective Q , the generalized eigenvalue problems (48) for design objective Q , the orthonormality constraint of the eigenvectors for design objective Q , the incremental state problem (36) of design objective Q for eigenvector directions, the incremental adjoint problem (37) of design objective Q for the directions of the eigenvectors, the adjoint problem (39) for chance constraint f , the generalized eigenvalue problems (48) for chance constraint f , the orthonormality constraint of the eigenvectors

tors for chance constraint f , the incremental state problem (41) of chance constraint f and the incremental adjoint problem (42) of chance constraint for the directions of the eigenvectors.

To compute the design gradient, we need to calculate five sets of functional derivatives to solve for the corresponding ten sets of adjoint variables $\{(\mathbf{u}^Q)^*, (\mathbf{u}^f)^*, (\mathbf{v}^Q)^*, (\mathbf{v}^f)^*, (\psi_j^Q)^*, (\psi_j^f)^*, (\hat{\mathbf{u}}_j^Q)^*, (\hat{\mathbf{u}}_j^f)^*, (\hat{\mathbf{v}}_j^Q)^*, (\hat{\mathbf{v}}_j^f)^*\}$ in (53), while the adjoint variable set for the eigenvalue set $\{\lambda_j^{Q*}, \lambda_j^{f*}\}$ is not required due to its independency of the design parameter d .

Setting the first variation of (53) with respect to the eigenvalue set $\{\lambda_j\}$ to zero isolates the terms corresponding to the quadratic approximation of the design objective and the orthonormality constraint of the eigenvectors, resulting in:

$$\{\psi_j^{Q*}\} = \left(\frac{1}{2} + \beta_V \lambda_j^Q\right) \{\psi_j^Q\}, \quad j = 1, \dots, N_{\text{eig}}^Q. \quad (54)$$

Setting the first variations of (53) to zero with respect to \mathbf{v}_j^Q and \mathbf{u}_j^Q results in the incremental state problem:

$$\text{Find } \hat{\mathbf{u}}^Q \in \mathcal{U}, \text{ such that } \langle \tilde{\mathbf{v}}, \partial_{\mathbf{v}\mathbf{u}} \bar{r}^Q (\mathbf{u}_j^Q)^* \rangle = -\langle \tilde{\mathbf{v}}, \partial_{\mathbf{v}m} \bar{r}^Q (\psi_j^Q)^* \rangle, \quad \forall \tilde{\mathbf{v}} \in \mathcal{V}. \quad (55)$$

and the incremental adjoint problem:

$$\begin{aligned} & \text{Find } \hat{\mathbf{v}}^Q \in \mathcal{V}, \text{ such that} \\ & \langle \tilde{\mathbf{u}}, \partial_{\mathbf{u}\mathbf{v}} \bar{r}^Q (\mathbf{v}_j^Q)^* \rangle = -\langle \tilde{\mathbf{u}}, \partial_{\mathbf{u}\mathbf{u}} \bar{r}^Q (\hat{\mathbf{u}}_j^Q)^* + \partial_{\mathbf{u}\mathbf{u}} \bar{Q} (\hat{\mathbf{u}}_j^Q)^* + \partial_{\mathbf{u}m} \bar{r}^Q (\psi_j^Q)^* \rangle, \quad \forall \tilde{\mathbf{u}} \in \mathcal{U}, \end{aligned} \quad (56)$$

similar to (36) and (37), respectively. In combination with (54), we can formulate the adjoint variables for the incremental state and adjoint problems individually for each eigenvector as

$$\{(\hat{\mathbf{u}}_j^*)\} = \left(\frac{1}{2} + \beta_V \lambda_j^Q\right) \{\hat{\mathbf{u}}_j^Q\}, \quad j = 1, \dots, N_{\text{eig}}^Q, \quad (57)$$

$$\{\hat{\mathbf{v}}_j^*\} = \left(\frac{1}{2} + \beta_V \lambda_j^Q\right) \{\hat{\mathbf{v}}_j^Q\}, \quad j = 1, \dots, N_{\text{eig}}^Q. \quad (58)$$

By vanishing the first variation of the Lagrangian functional (53) with respect

to the adjoint or the state, we obtain the linear state problem: *Find* $\mathbf{u}^Q \in \mathcal{U}$, *such that*

$$\begin{aligned}
\langle \tilde{\mathbf{v}}, \partial_{\mathbf{v}\mathbf{u}} \bar{r}^Q (\mathbf{u}^Q)^* \rangle &= -2\beta_V \langle \tilde{\mathbf{v}}, \partial_{\mathbf{v}m} \bar{r}^Q (\mathcal{C} \partial_m \bar{r}^Q) \rangle \\
&- \sum_{j=1}^{N_{\text{eig}}^Q} \langle \tilde{\mathbf{v}}, \partial_{\mathbf{v}mu} \bar{r}^Q \hat{\mathbf{u}}_j^Q (\psi_j^Q)^* + \partial_{\mathbf{v}mm} \bar{r}^Q \psi_j^Q (\psi_j^Q)^* \rangle \\
&- \sum_{j=1}^{N_{\text{eig}}^Q} \langle \tilde{\mathbf{v}}, \partial_{\mathbf{v}uu} \bar{r}^Q \hat{\mathbf{u}}_j^Q (\hat{\mathbf{u}}_j^Q)^* + \partial_{\mathbf{v}um} \bar{r}^Q \psi_j^Q (\hat{\mathbf{u}}_j^Q)^* \rangle, \quad \forall \tilde{\mathbf{v}} \in \mathcal{V},
\end{aligned} \tag{59}$$

and linear adjoint problem: *Find* $(\mathbf{v}^Q)^* \in \mathcal{V}$, *such that*

$$\begin{aligned}
\langle \tilde{\mathbf{u}}, \partial_{\mathbf{u}\mathbf{v}} \bar{r}^Q (\mathbf{v}^Q)^* \rangle &= -\langle \tilde{\mathbf{u}}, \partial_{\mathbf{u}} \bar{Q} \rangle - 2\beta_V \langle \tilde{\mathbf{u}}, \partial_{\mathbf{u}m} \bar{r}^Q (\mathcal{C} \partial_m \bar{r}^Q) \rangle \\
&- \langle \tilde{\mathbf{u}}, \partial_{\mathbf{u}\mathbf{u}} \bar{r}^Q (\mathbf{u}^Q)^* + \partial_{\mathbf{u}\mathbf{u}} \bar{Q} (\mathbf{u}^Q)^* \rangle \\
&- \sum_{j=1}^{N_{\text{eig}}^Q} \langle \tilde{\mathbf{u}}, \partial_{\mathbf{u}mv} \bar{r}^Q \hat{\mathbf{v}}_j (\psi_j^Q)^* \\
&+ \partial_{\mathbf{u}mu} \bar{r}^Q \hat{\mathbf{u}}_j (\psi_j^Q)^* + \partial_{\mathbf{u}mm} \bar{r}^Q \psi_j^Q (\psi_j^Q)^* \rangle \\
&- \sum_{j=1}^{N_{\text{eig}}^Q} \langle \tilde{\mathbf{u}}, \partial_{\mathbf{u}vu} \bar{r}^Q \hat{\mathbf{u}}_j^Q (\hat{\mathbf{v}}_j^Q)^* + \partial_{\mathbf{u}vm} \bar{r}^Q \psi_j^Q (\hat{\mathbf{v}}_j^Q)^* \rangle \\
&- \sum_{j=1}^{N_{\text{eig}}^Q} \langle \tilde{\mathbf{u}}, \partial_{\mathbf{u}uv} \bar{r}^Q \hat{\mathbf{v}}_j^Q (\hat{\mathbf{u}}_j^Q)^* + \partial_{\mathbf{u}uu} \bar{r}^Q \hat{\mathbf{u}}_j^Q (\hat{\mathbf{u}}_j^Q)^* \\
&+ \partial_{\mathbf{u}uu} \bar{Q} \hat{\mathbf{u}}_j^Q (\hat{\mathbf{u}}_j^Q)^* + \partial_{\mathbf{u}uum} \bar{r}^Q \psi_j^Q (\hat{\mathbf{u}}_j^Q)^* \rangle, \\
&\forall \tilde{\mathbf{u}} \in \mathcal{U}.
\end{aligned} \tag{60}$$

By vanishing the first variation of (53) with respect to the eigenvalue set $\{\lambda_j^f\}$, we get

$$\{(\psi_j^f)^*\} = \left(\frac{1}{2} + \beta_V \lambda_j^f \right) \{\psi_j^f\}, \quad j = 1, \dots, N_{\text{eig}}^f. \tag{61}$$

Equating to zero of the first variations of (53) with respect to \mathbf{v}_j^f and \mathbf{u}_j^f results in the incremental state problem:

$$\textit{Find } \hat{\mathbf{u}}^f \in \mathcal{U}, \textit{ such that } \langle \tilde{\mathbf{v}}, \partial_{\mathbf{v}\mathbf{u}} \bar{r}^f \mathbf{u}_j^{f*} \rangle = -\langle \tilde{\mathbf{v}}, \partial_{\mathbf{v}m} \bar{r}^f \psi_j^{f*} \rangle, \quad \forall \tilde{\mathbf{v}} \in \mathcal{V}. \tag{62}$$

and linear adjoint problem:

Find $(\mathbf{v}^f)^* \in \mathcal{V}$, such that

$$\begin{aligned}
\langle \tilde{\mathbf{v}}, \partial_{\mathbf{uv}} \bar{r}^f (\mathbf{u}^f)^* \rangle &= - \sum_{n=1}^{N_{\text{eig}}^f} \langle \tilde{\mathbf{v}}, \partial_{\mathbf{v}m\mathbf{u}} \bar{r}^f \hat{\mathbf{u}}_n^f (\psi_n^f)^* + \partial_{\mathbf{v}mm} \bar{r}^f \psi_n^f (\psi_n^f)^* \rangle \\
&\quad - \sum_{n=1}^{N_{\text{eig}}^f} \langle \tilde{\mathbf{v}}, \partial_{\mathbf{v}\mathbf{u}\mathbf{u}} \bar{r}^f \hat{\mathbf{u}}_n^f (\hat{\mathbf{u}}_n^f)^* + \partial_{\mathbf{v}\mathbf{u}m} \bar{r}^f \psi_n^f (\hat{\mathbf{u}}_n^f)^* \rangle \\
&\quad - \langle \tilde{\mathbf{v}}, \partial_{\mathbf{v}m} \bar{r}^f m^f \rangle \\
&\quad \forall \tilde{\mathbf{u}} \in \mathcal{U}.
\end{aligned} \tag{63}$$

Finally, with driving all the adjoint variables, the d -gradient is derived as

$$\langle \tilde{d}, D_d \mathcal{J}_{\text{QUAD}}(d) \rangle = \langle \tilde{d}, \partial_d \mathcal{L}_{\text{QUAD}} \rangle. \tag{64}$$

The methodology for calculating the design gradient is detailed in Algorithm 2. The computational cost required to evaluate the quadratic approximation of the cost functional, denoted as $\mathcal{J}_{\text{QUAD}}(d)$ in (52), includes solving one potentially nonlinear state partial differential equation (PDE), one linear adjoint problem, and $2(N_{\text{eig}}^Q + N_o) + 2(N_{\text{eig}}^f + N_o) + 2$ linear PDEs, as prescribed by the double-pass randomized algorithm presented in Algorithm 1. Furthermore, obtaining the d -gradient involves solving $2(N_{\text{eig}}^Q + N_{\text{eig}}^f + 3)$ additional linear PDEs.

5. Numerical Results

This section presents numerical experiments utilizing the proposed design under uncertainty framework for beam-insulation scenario in Figure 1 in both 2D and 3D. The objective is to achieve thermal insulation and mechanical stability avoiding stress concentration while mitigating uncertainty in the design process. The analyses presented in this section, investigate the accuracy and convergence of quadratic and Monte Carlo approximation of design objective and explores the effect of different limiting critical stress, critical chance, and uncertain parameter variance and spatial correlation on the optimal design, spatial pattern of d_{opt} , as well as the probability distributions

Algorithm 2: Analytical design gradient

Input : Design objective (12) and weak form of the PDF (7).

Output: Gradient of the quadratic approximation of the design objective $\mathcal{J}_{\text{QUAD}}(d)$ with respect to the design parameter z .

- 1 Solve for m -gradient (34);
 - 2 Solve for m -Hessian (38);
 - 3 Solve for m_f -gradient ;
 - 4 Solve for m_f -Hessian ;
 - 5 Solve for generalized eigenpairs with Algorithm 1;
 - 6 Compute $\mathcal{J}_{\text{QUAD}}$ by (52);
 - 7 Solve the linear state problem (59);
 - 8 Solve the linear adjoint problem (63);
 - 9 Obtain the design gradient (64)
-

of the design objectives Q . The parameters of the forward model are summarized in Table 1. The computational implementation of the framework relies on several open-source libraries like FEniCS [56] for the finite element solution of the forward model, SOUPy [57] for the quadratic approximation of the design objective and implementation of chance constraint, and HIPPYLib [54] for the Gaussian random field, trace estimator and INCG optimizer.

Parameter	Value
κ_s	0.477 W/mK
κ_f	0.085 W/mK
κ_b	5 W/mK
α_T	10^{-5} (1/K)
h	81059 W/m ² K
D	0.25×10^{-8} Pa
λ	6.77 GPa
μ	3.38 GPa
λ_b	17.3 GPa
μ_b	11.5 GPa

Table 1: List of the forward model parameters and their values used in the design problem.

5.1. Spatially-correlated uncertain parameter

Figure 4 highlights the effect of the uncertain parameter m , derived from an

anisotropic Gaussian random field described in equation (10), on the porosity field. This figure provides an illustrative example of porosity design, accompanied by two sets of porosity samples generated based on the samples of m

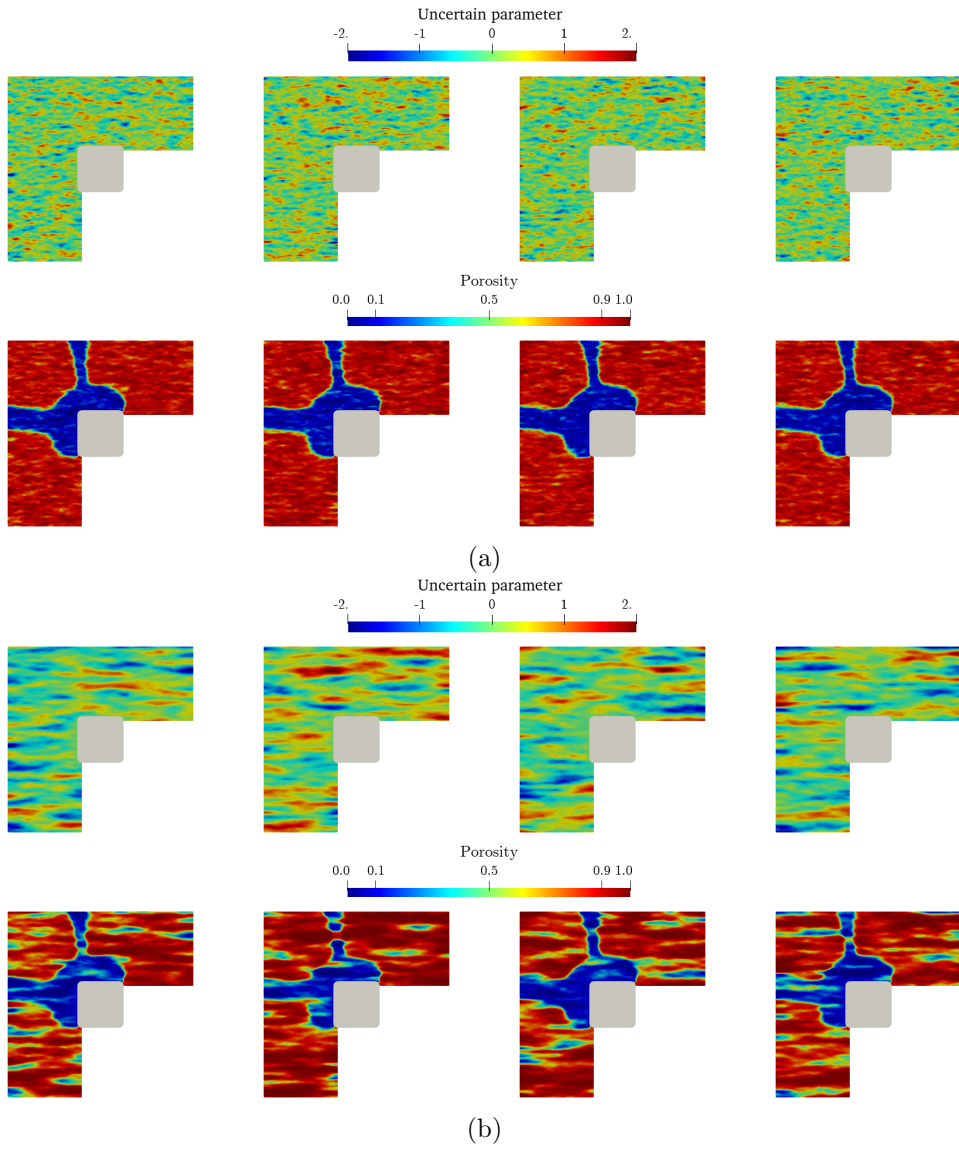


Figure 4: Samples of uncertain parameter m and its effect on the aerogel porosity field $\phi_f(\mathbf{x})$ for two cases: (a) Correlation length $L_c = 0.05$ and variance of $\sigma^2 = 0.25^2$ and (b) Correlation length $L_c = 0.25$ and variance of $\sigma^2 = 0.5^2$. The mean of the uncertain parameter is $\tilde{m} = 0$ and anisotropy is $\vartheta_x = 1, \vartheta_y = 1 \times 10^{-4}$ for both cases.

and the map defined in (9). The mean of the uncertain parameter $\tilde{m} = 0$ and anisotropy is $\vartheta_x = 1, \vartheta_y = 1 \times 10^{-4}$. Figure 4 (a) has a correlation length of $L_c = 0.05$ and variance of $\sigma^2 = 0.25^2$, whereas Figure 4 (b) has a correlation length of $L_c = 0.25$ and variance of $\sigma^2 = 0.5^2$. As the correlation length of m increases, a pronounced anisotropy in the material porosity becomes evident, as shown in Figure 4 (a) and (b). This anisotropic behavior serves as an effective representation of the horizontal layer-by-layer manufacturing process, reflecting both the correlation of aerogel properties within individual layers and the distinctive characteristics across different layers.

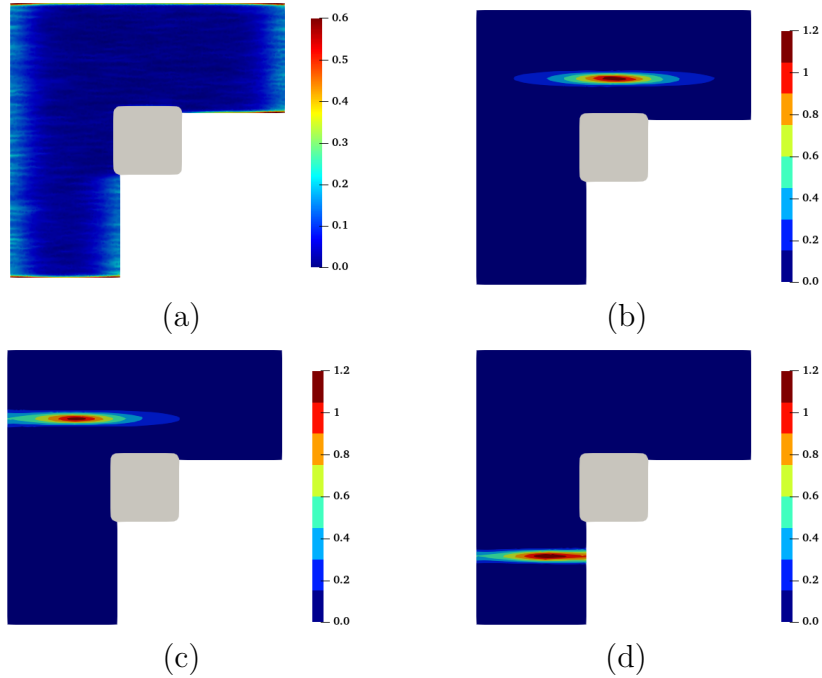


Figure 5: The effect of boundary on the Gaussian random field in (11) for the scenario used in Figure 7: (a) marginal variance of the anisotropic uncertain parameter m , and point-wise correlation structure centered at (b) point $(0.5, 0.75)$ (c) point $(0.25, 0.75)$ (d) point $(0.25, 0.25)$. Coordinates (x, y) are defined with respect to the bottom left corner of the beam-insulator domain. The uncertain parameter m is characterized by a mean value of $\tilde{m} = 0$, a variance of $\sigma^2 = 0.5^2$ and a correlation length of $L_c = 0.25$.

To evaluate the performance of the Robin boundary condition in minimizing boundary effects on a Gaussian random field characterized by Matérn covariance, as defined in (10), we analyze the diagonal components of the discretized covariance operator \mathcal{C} . Figure 5 represents the exact marginal

variance of the anisotropic uncertain parameter m . A slight deviation from uniform variance is observed, particularly in the blue-shaded areas near the horizontal boundaries, which span approximately 8% of the domain. This indicates a relatively minor boundary effect. The application of Robin boundary conditions with a constant coefficient, as discussed in Section 2.2, effectively mitigates this effect. The horizontal noise visible in the figure arises from assigning a low anisotropy value to the anisotropic tensor in equation (11) to ensure numerical stability. Furthermore, Figures 5(b)–(d) present spatial correlation patterns at three distinct locations in the domain, revealing nearly undistorted elliptical contours, which ensure that boundary effects are minimal in this setting.

5.2. Quadratic and Monte Carlo approximations

To assess the accuracy and efficiency of the quadratic approximation and Monte Carlo estimations of mean and variance of design objective with a control variate on the optimal design solution, we perform comparative analyses. As the sample size and number of dominant eigenvalues increase, both methods converge to similar mean and variance values, consistent with standard Monte Carlo estimations, as shown in Figure 6. For large sample sizes, the estimated mean and variance from the standard Monte Carlo method (Figure 6(a)) and the Monte Carlo method with control variate (Figure 6(b)) are nearly identical. However, the quadratic approximation as a control variate achieves lower error bounds with significantly fewer samples, as evident in the box plots. Furthermore, with only $N_{tr} = 25$ trace estimators, the quadratic approximation closely matches the Monte Carlo results (Figure 6(c)), leading to significant savings in computational cost without loss in accuracy.

Figures 7 and 8 compare the effects of different variances and correlation lengths of the uncertain parameter m on the optimal design d_{opt} indicating the spatial distribution of aerogel porosity and the probability distributions of the design objective Q representing the thermal insulation performance of the thermal break. The optimal design is evaluated using standard Monte Carlo, Monte Carlo with control variate, and a quadratic Taylor approximation of the mean and variance of Q . In Figure 7 (low variance and short correlation length), the morphologies of d_{opt} and probability distributions of Q are nearly identical across all three methods. However, in Figure 8 (high variance and long correlation length), the quadratic approximation predicts different optimal design pattern with higher Q , while Monte Carlo with control variate yields results closely matching standard Monte Carlo but with

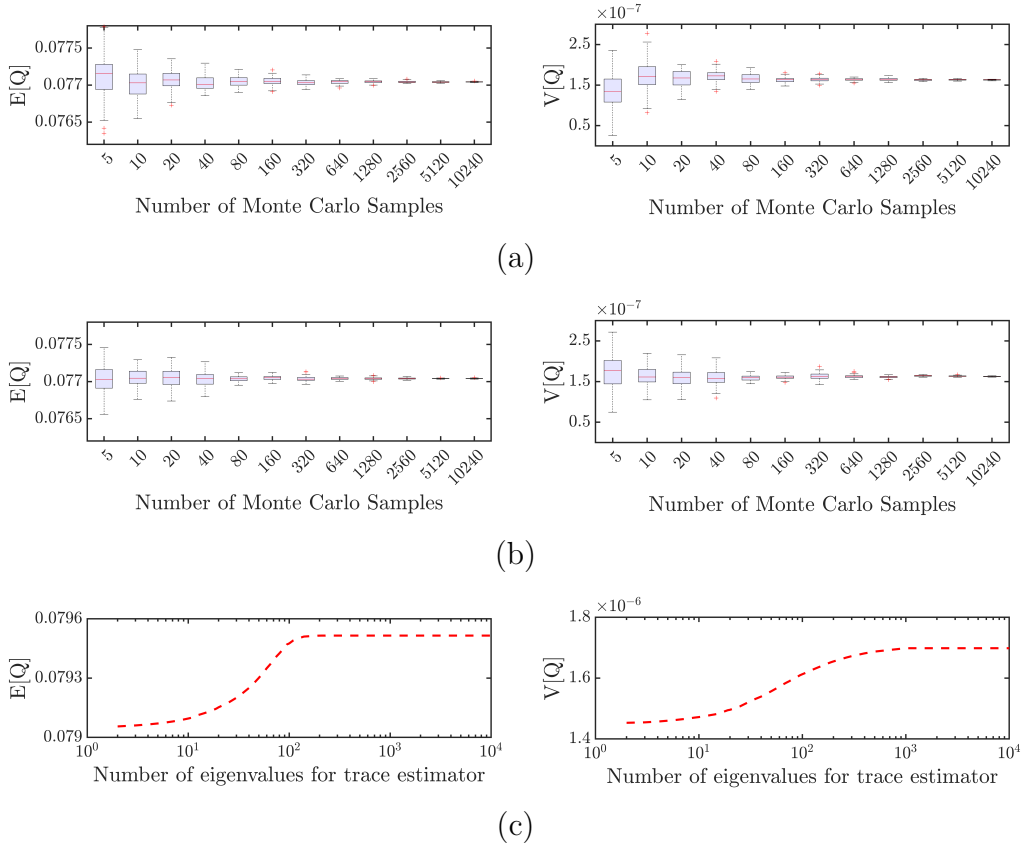


Figure 6: Convergence plots corresponding to scenario in Figure 7 for the mean and variance of the design objective Q : (a) standard Monte Carlo method (b) Monte Carlo with control variate and (c) Quadratic approximation. The uncertain parameter m has the correlation length $L_c = 0.05$ and a variance of $\sigma^2 = 0.25^2$.

significantly fewer samples (PDF solved). Interestingly, while the spatial pattern of the optimal design in Figure 7 appears nearly symmetric, the higher uncertainty in Figure 8 results in optimal designs that consistently position stronger material (lower aerogel porosity) along the horizontal axis, across all three approximation methods. This pattern reflects the anisotropy of the uncertain parameter, modeled with a higher correlation length along the layer deposition direction (see Figure 4). Also, the optimal designs at mean $\tilde{m} = 0$ are much similar in Figure 7 as compared to Figure 8 where there is a deviation in the design patterns, which shows that there is a trade-off favoring the reduction of the uncertainty over mean performance for our design formulation (12). These results demonstrate that the proposed optimiza-

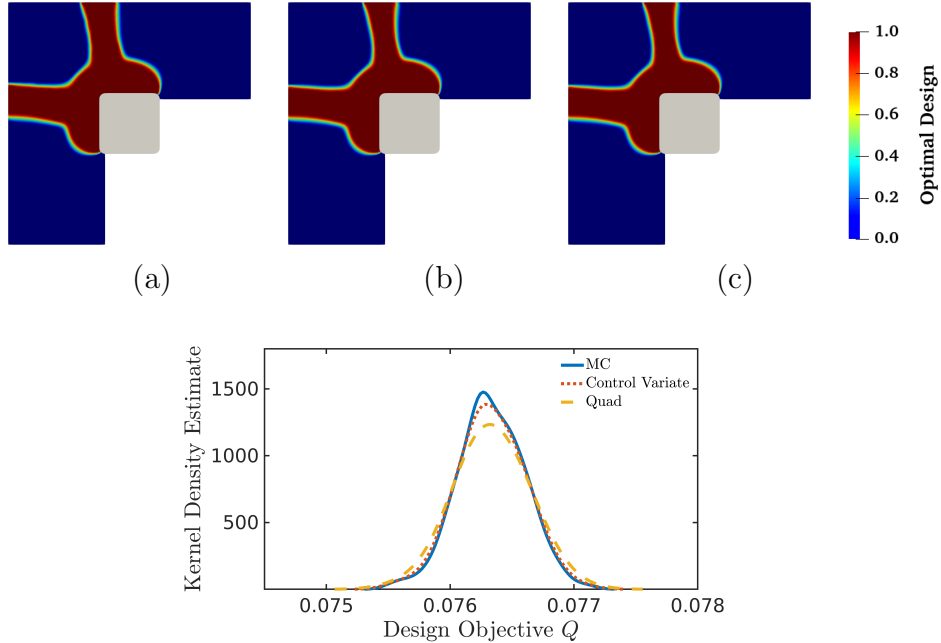


Figure 7: The top row shows the optimal design obtained for $\sigma = 0.25$ for the three different approaches: (a) Sampled Average approximation (500 samples) (b) Monte Carlo correction (100 samples) and (c) Quadratic approximation ($N_{tr} = 25$). The bottom row shows the QoI distribution of the design objective Q for the three different cases above. The uncertain parameter m has a correlation length $L_c = 0.05$ for all three cases.

tion under uncertainty framework effectively captures spatial uncertainty, producing more reliable design solutions.

5.3. Scalability with respect to number of design parameters

We assess the scalability of the algorithm for PDE-constrained optimization under uncertainty with respect to the design dimension, determined by the number of nodes in the spatial discretization of d , and governed by two primary factors: Firstly, the eigenvalue decay rate of the covariance-preconditioned Hessian, estimated via the randomized trace estimator, and secondly the convergence behavior of the INCG optimizer. Figure 9 illustrates the behavior of the chance constraint function in (14) with the number of steps in the continuation scheme, the gradient norm 64 and the absolute values of the generalized eigenvalues 48 for the last step of chance convergence discussed in Algorithm 3. These metrics are presented for two design parameter dimensions, corresponding to the optimal design problem depicted

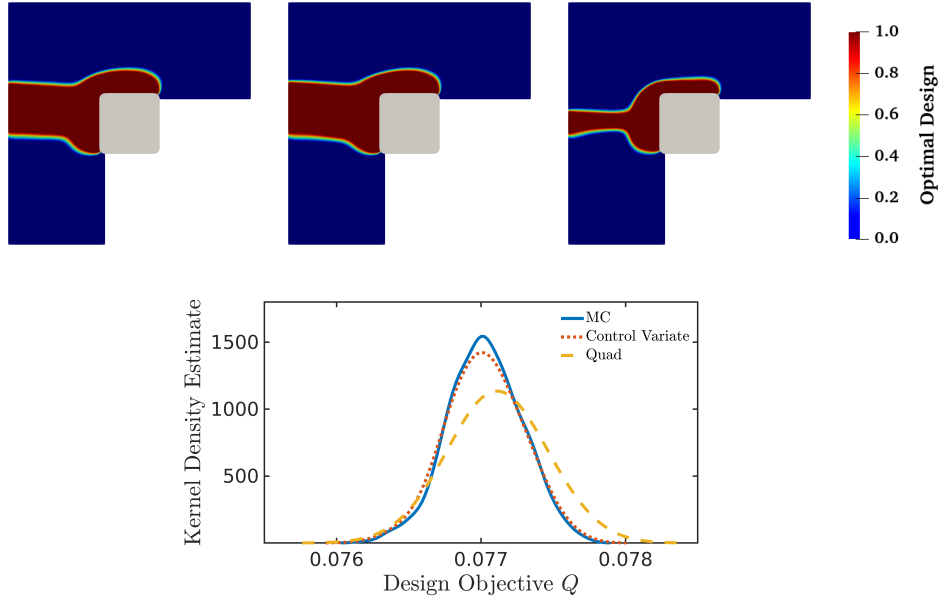


Figure 8: The top row shows the optimal design obtained for $\sigma = 0.5$ for the three different approaches: (a) standard Monte Carlo using 500 samples, (b) Monte Carlo with control variate using 100 samples, and (c) Quadratic approximation using $N_{tr} = 25$. The bottom row shows the QoI distribution of the design objective Q for the three different cases above. The uncertain parameter m has a correlation length of $L_c = 0.25$ for all three cases.

in Figure 7 (c). These results demonstrate that the quadratic approximation enables rapid decay of the critical chance, with the gradient norm converging below the tolerance threshold within 100 iterations for both mesh resolutions. The minimal dependence of convergence on mesh resolution highlights that the gradient-based INCG optimizer is effectively independent of the number of uncertain parameters. Additionally, Figure 9(c) shows a rapid eigenvalue decay, unaffected by the dimension of uncertain parameters, supporting the scalability of the randomized eigensolver used for trace approximation. Figure 10 depicts the eigenfunctions of the covariance-preconditioned Hessian for the design objective. Eigenvectors associated with larger eigenvalues capture broader spatial scales of the design parameter, while those linked to smaller eigenvalues become increasingly oscillatory and less significant. Together, these dimension-independent factors suggest that leveraging quadratic Taylor approximations and stochastic optimization techniques enables a scalable approach for PDE-constrained optimal design under uncertainty with the enforcement of chance constraints, regardless of the dimensionality of the

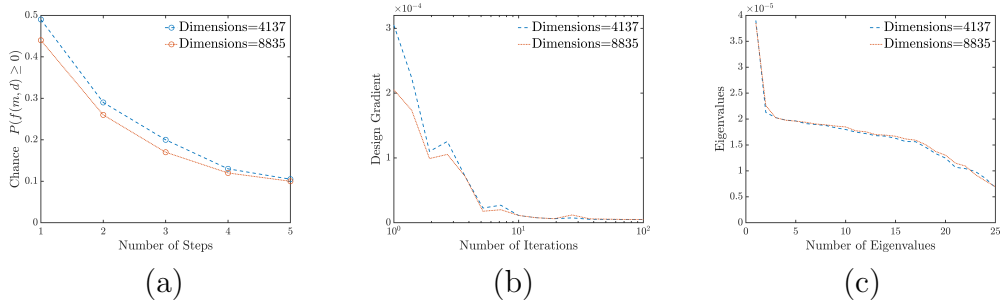


Figure 9: Optimization solution corresponding to Figure 7 (c) for different dimensions of design parameter: (a) Convergence of the chance $P(f(m, d) \geq 0)$ with the number of steps, (b) convergence of the norm of the design gradient with number of iterations of INCG optimizer, (c) eigenvalue decay of the covariance-preconditioned Hessian

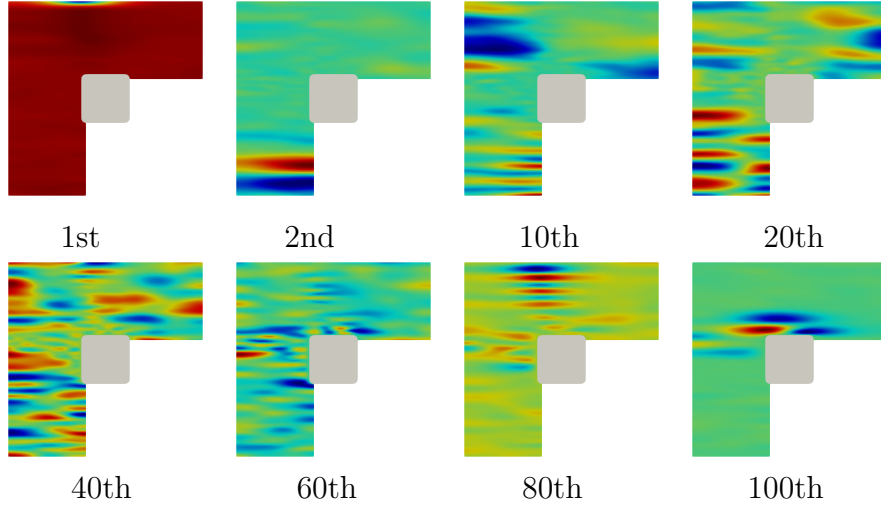


Figure 10: Eigenfunctions of the covariance-preconditioned Hessian of the design objective corresponding to eigenvalue decay for the scenario in Figure 7 (c).

uncertain parameters.

5.4. Optimal design: effect of chance constraint

The chance constraint function defined in (14) incorporates parameters such as α_c and T_{cr} , which govern the enforcement of constrain to mitigate stress concentrations within the domain. In particular, the probability of chance $P(f(m, d) \geq 0)$ is limited by a threshold α_c , where the function f is the difference between the limiting critical stress T_{cr} and the p-norm of the

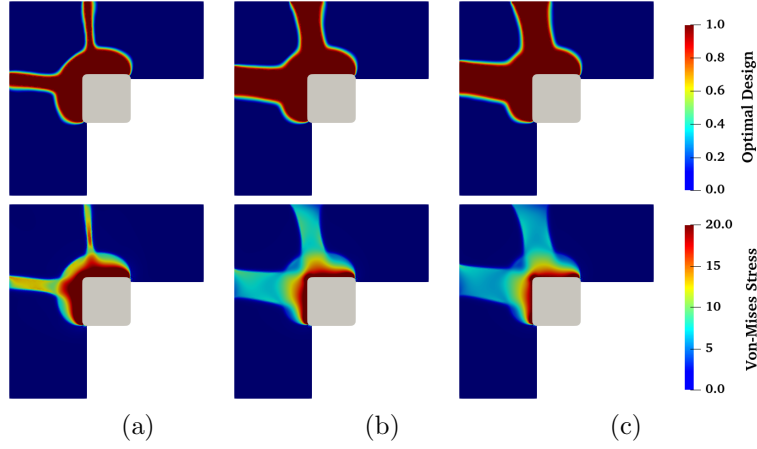


Figure 11: The top row shows the optimal design results obtained at the mean of the uncertain sample $\tilde{m} = 0$ for different values of critical chance: (a) $\alpha_c = 0.05$ (b) $\alpha_c = 0.08$ and (c) $\alpha_c = 0.1$. The bottom row represents the von Mises stress for the corresponding optimal designs in the top row. In all results $T_{cr} = 22.5\text{MPa}$, $L_c = 0.25$, $\sigma = 0.25$, $\beta_V = 0.1$ and $\beta_R = 1 \times 10^{-5}$.

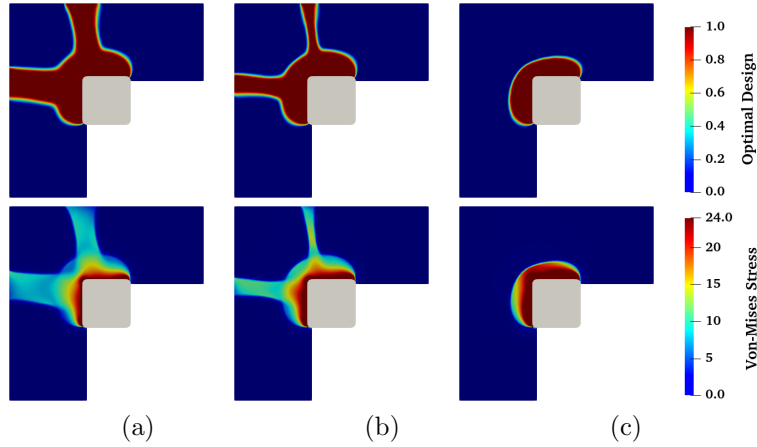


Figure 12: The top row shows the optimal design results obtained at the mean of the uncertain sample $\tilde{m} = 0$ for different values of limiting critical stress: (a) $T_{cr} = 20\text{MPa}$ (b) $T_{cr} = 22.5\text{MPa}$ and (c) $T_{cr} = 25\text{MPa}$. The bottom row represents the von Mises stress for the corresponding optimal designs in the top row. In all results $\alpha_c = 0.05$, $L_c = 0.25$, $\sigma = 0.25$, $\beta_V = 0.1$ and $\beta_R = 1 \times 10^{-5}$.

von Mises stress T_{pn} . To examine the influence of α_c on optimal design, a parametric study was conducted with constant parameters, as shown in Figure 11. The critical stress limit was set at $T_{cr} = 22.5\text{MPa}$, while α_c was varied among 0.05, 0.08, and 0.1. This figure presents the optimal design, and von

Mises stress distribution evaluated at the mean of the uncertain parameter $\tilde{m} = 0$. The results indicate that increasing critical chance α_c expands the regions of mechanically stronger material (highlighted in red), effectively reducing localized stresses across the component. However, this improvement in mechanical stability comes at the expense of insulation performance of the thermal break.

The limiting critical stress, T_{cr} , defines the maximum permissible von Mises stress within the beam structure. Figure 12 demonstrates the influence of T_{cr} on the optimal designs, evaluated at the mean of the uncertain parameter $\tilde{m} = 0$, along with the corresponding von Mises stress distributions. The findings indicate that increasing the critical stress T_{cr} results in the allocation of stronger insulating material (depicted in blue) across a larger region of the domain. This enhances the insulation performance but compromises the mechanical strength of the component. Thus, a higher value of T_{cr} improves insulation efficiency at the expense of reduced mechanical stability. Figure 13 shows the state parameters and porosity field evaluated at the mean of the uncertain parameter $\tilde{m} = 0$ and three samples for the optimal design in Figure 12 (b). The states include the solid displacement magnitude $\|\mathbf{u}_s\|$, magnitude of effective solid stress $\|\mathbf{T}_s\|$, solid temperature θ_s , fluid temperature θ_f and fluid pressure p .

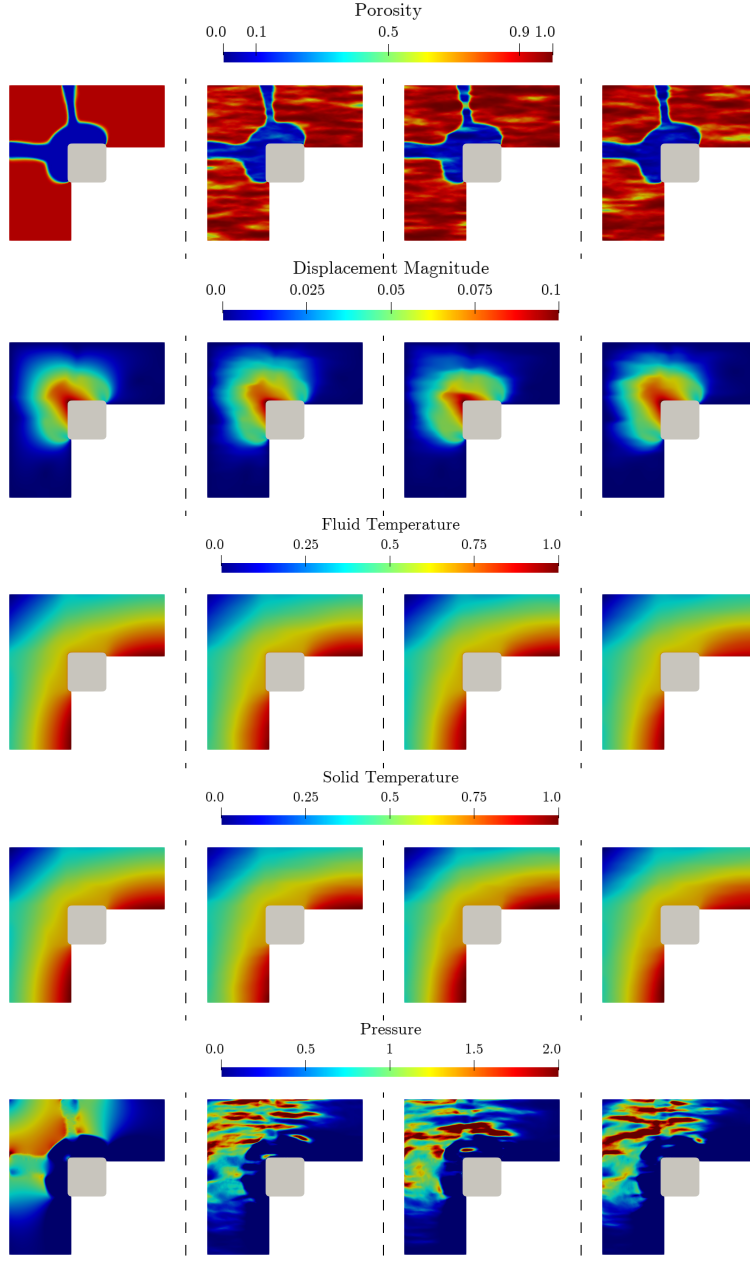


Figure 13: Porosity and states of the scenario at the optimal design shown in Figure 11 (b) obtained at the mean (first column) of the uncertain parameter $\hat{m} = 0$, three i.i.d. samples (second, third and fourth column) of m . The rows show the porosity ϕ_f , solid displacement magnitude $\|\mathbf{u}_s\|$, magnitude of effective solid stress $\|\mathbf{T}_s\|$, solid temperature θ_s , fluid temperature θ_f and fluid pressure p .

5.5. Three-dimensional design of beam-insulator system

We demonstrate the efficiency and scalability of the proposed optimization

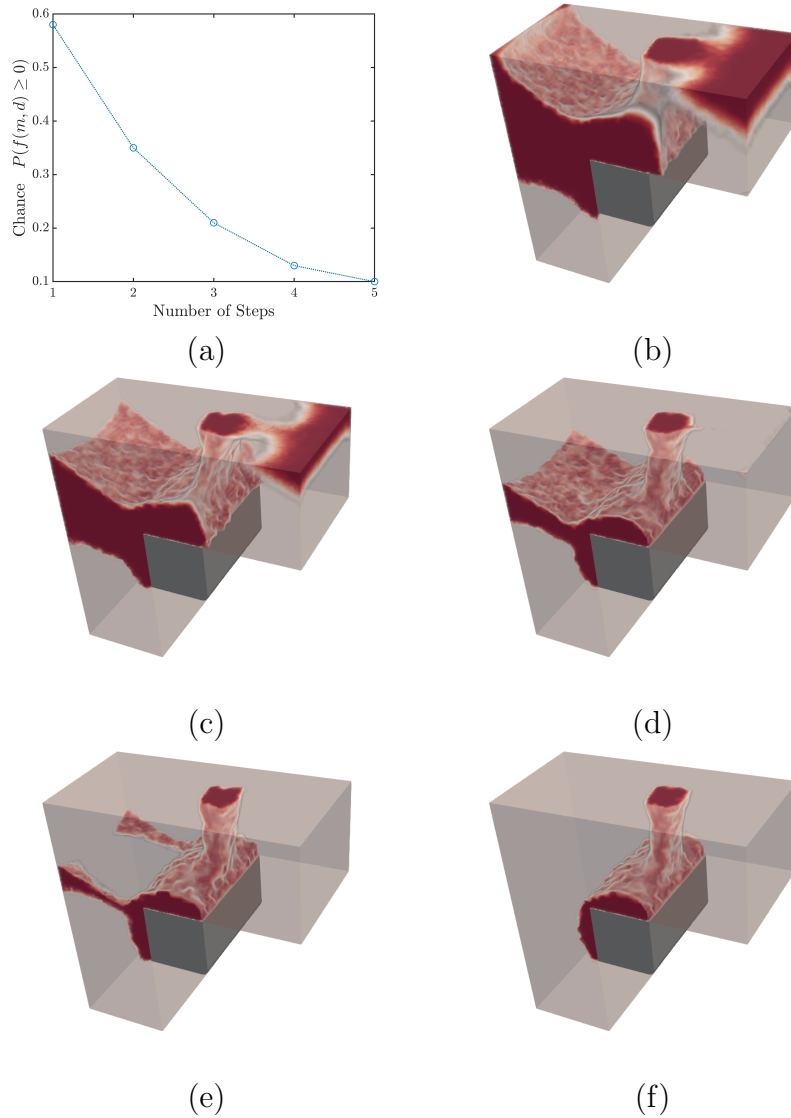


Figure 14: Convergence of critical chance α_c with the results obtained for optimal design at mean $\tilde{m} = 0$ for steps in adaptive optimization discussed in Algorithm 3 from step 1 to step 5 shown in (b)-(f). The uncertain parameter m has a correlation length of $L_c = 0.25$ and a variance of $\sigma^2 = 0.1^2$, the critical chance is $\alpha_c = 0.1$, and the critical stress considered is $T_{cr} = 15$ MPa.

under uncertainty framework by applying it to a three-dimensional design

problem. Specifically, we consider the 3D thermal break scenario shown in Figure 1, with a thickness of 0.5. In this case, a uniform circular load is also applied to the middle of the top surface, simulating the influence of additional building envelope assemblies. The uncertain parameter m is modeled with a horizontal correlation length of $L_c = 0.25$ and a variance of $\sigma^2 = 0.1^2$. For the chance constraint, we set a critical chance of $\alpha_c = 0.1$ and a critical stress of $T_{cr} = 15$ MPa. The finite element discretization of the 3D domain resulted in 389,044 design parameters. Figure 14 illustrates the optimal designs obtained

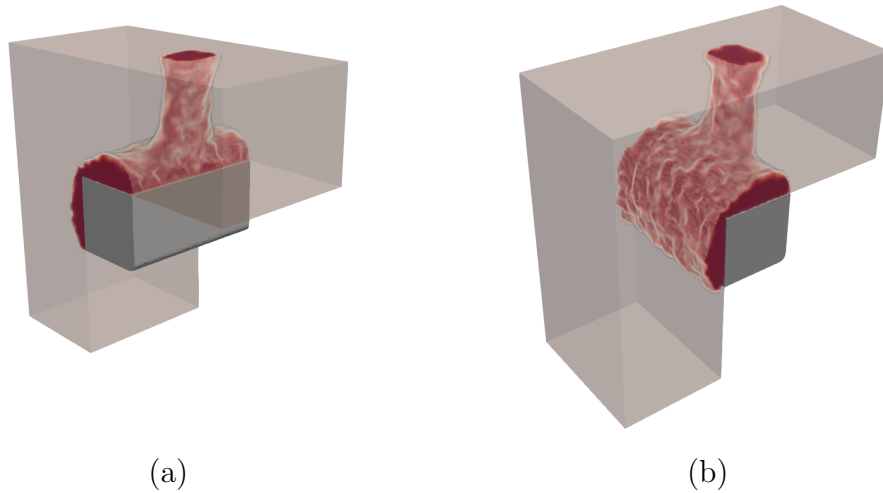


Figure 15: Final design obtained after five steps of the continuation scheme, achieving convergence of the critical chance α_c . The 3D domain's finite element discretization, resulted in 389044 design parameters.

at each step of the continuation scheme outlined in Algorithm 3. Regions shown in red correspond to material with low porosity ($\phi_f = 0.1$). As the continuation scheme progresses, the red regions gradually decrease, reducing mechanical support in the domain and increasing the p-norm of von Mises stress. Consequently, the probability in (14) approaches the critical chance threshold of $\alpha_c = 0.1$. By step 5, the final design, shown in Figure 15, emerges, featuring a column-like structure of low-porosity material $\phi_f = 0.1$, providing support aligned with the direction of the applied external load.

6. Conclusions

This study introduces an efficient and scalable computational framework for chance-constrained optimal design under high-dimensional uncertainty gov-

erned by partial differential equations (PDEs). The framework optimizes the spatial distribution of a spatially correlated and uncertain porosity field in additively manufactured aerogel thermal breaks to maximize thermal insulation performance while mitigating stress concentrations. Two key strategies are implemented within the framework. The first utilizes a quadratic Taylor expansion of the design objective with respect to the uncertain parameters to efficiently estimate the mean and variance in the cost function, as well as the chance constraints. The second employs the quadratic approximation as a control variate to enhance the efficiency of Monte Carlo estimations. The framework incorporates a randomized algorithm to solve the generalized eigenvalue problem, enabling efficient computation of the trace of the covariance-preconditioned Hessian. Scalability with respect of high-dimensional uncertain parameter is achieved through the rapid decay of eigenvalues and the dimension-independent convergence of the optimization iterations.

In future work, we aim to enhance the current design framework under uncertainty by incorporating uncertainties in the forward model parameters. These uncertainties can be rigorously quantified using Bayesian inference methods informed by experimental measurements of aerogel properties. Additionally, our present results demonstrate effective control over interface thickness between materials using Tikhonov regularization. To further improve control for a broader range of design scenarios, we plan to integrate phase-field regularization, as proposed in [31]. This enhancement would be implemented through a continuation scheme, which, while potentially increasing computational demands, offers improved precision in interface control. Finally, despite the efficiency of the existing framework, its application to large-scale engineering systems remains computationally challenging due to the extensive requirement for repeated PDE solves within the optimization loop. To overcome this limitation, we propose incorporating a Bayesian neural operator surrogate model for the multiphase PDE system, following the construction methodology outlined in [58]. This surrogate model would ensure reliable predictions by accurately capturing the relationship between joint uncertainties and design parameters. Furthermore, it would enable efficient approximation of both the PDE state and its sensitivities with respect to the design parameters, facilitating scalable and computationally feasible gradient-based optimization for complex systems.

This study addresses the computational challenges of PDE-constrained optimization under high-dimensional uncertainty by leveraging intrinsic di-

mensionality and incorporating chance constraints to prevent stress concentrations. The framework enhances optimal design reliability, offering a robust and scalable approach while paving the way for future advancements to refine and extend its capabilities.

Acknowledgments

The authors gratefully acknowledge the financial support received from the U.S. National Science Foundation (NSF) CAREER Award CMMI-2143662. The authors express their appreciation for the helpful discussions with Dr. Peng Chen, from Georgia Institute of Technology, regarding the problem formulation and software libraries. Additionally, the authors would like to acknowledge the support provided by the Center for Computational Research at the University at Buffalo.

Appendix A. Adaptive optimization

The gradient-based scheme uses a continuation scheme that gradually in-

Algorithm 3: Adaptive Optimization

Input : Initial design parameter d_0 , smoothing parameter ω_0 ,
penalty parameter γ_0 , power parameters σ_ω and σ_γ ,
 $\hat{f} = f_{\text{QUAD}}(d)$

Output: Design gradient d_{opt}

- 1 **while** $\|d_k - d_{k-1}\| \leq \epsilon_{\text{out}}$ or $k < k_{\text{max}}$;
 $d_{k+1} = \text{Inexact Newton Conjugate-Gradient}(d_k, \mathcal{J}(d), \nabla_d \mathcal{J}(d), \epsilon_{\text{in}})$;
Evaluate approximate chance \hat{f}_{k+1} at d_{k+1} ; Update $\omega_{k+1} = \sigma_\omega \omega_k$,
 $\gamma_{k+1} = \sigma_\gamma \gamma_k$;
- 2 **end while**
- 3 Obtain the design gradient d_{opt} ;

creases the smoothing parameter ω and penalty parameter γ to achieve convergence [25]. An initial value of the smoothing parameter ω_0 and the penalty parameter γ_0 is defined for the continuation scheme. These parameters are updated at the end of each iteration using scaling parameters σ_ω and σ_γ for smoothing and penalty parameters, respectively. For k^{th} iteration, the updated smoothing parameter is $\omega_{k+1} = \sigma_\omega \omega_k$ and the updated penalty parameter is $\gamma_{k+1} = \sigma_\gamma \gamma_k$. In an outer loop, we update the parameters ω and

γ , whereas an Inexact Newton Conjugate-Gradient (INCG) is applied in the inner loop to solve the optimization problem (51). The termination criterion for the outer loop is if the maximum number of iterations k_{\max} is reached. For each iteration, the approximated chance is computed through the quadratic approximation f_{QUAD} of the chance function as given in (14). The output is the optimal value of design parameter d_{opt} . The algorithm for this adaptive optimization is given in Algorithm 1.

Bibliography

- [1] L. An, B. Liang, Z. Guo, J. Wang, C. Li, Y. Huang, Y. Hu, Z. Li, J. N. Armstrong, C. Zhou, et al., Wearable aramid–ceramic aerogel composite for harsh environment, *Advanced Engineering Materials* 23 (3) (2021) 2001169.
- [2] Z. Guo, R. Yang, T. Wang, L. An, S. Ren, C. Zhou, Cost-Effective Additive Manufacturing of Ambient Pressure-Dried Silica Aerogel, *Journal of Manufacturing Science and Engineering* 143 (1) (2020) 011011. doi:10.1115/1.4048740.
- [3] L. An, M. Di Luigi, J. Tan, D. Faghihi, S. Ren, Flexible percolation fibrous thermal insulating composite membranes for thermal management, *Materials Advances* 4 (1) (2023) 284–290.
- [4] S. Zhao, G. Siqueira, S. Drdova, D. Norris, C. Ubert, A. Bonnin, S. Galmarini, M. Ganobjak, Z. Pan, S. Brunner, et al., Additive manufacturing of silica aerogels, *Nature* 584 (7821) (2020) 387–392.
- [5] D. Topuzi, Structural thermal breaks, <https://www.structuremag.org/> (2020).
- [6] S. Hamel, K. Peterman, Thermal breaks in building envelopes, <https://www.structuremag.org/article/thermal-breaks-in-building-envelopes/> (2019).
- [7] C. Woischwill, I. Y. Kim, Multimaterial multijoint topology optimization, *International Journal for Numerical Methods in Engineering* 115 (13) (2018) 1552–1579.

- [8] J. Guilleminot, A. Asadpoure, M. Tootkaboni, Topology optimization under topologically dependent material uncertainties, *Structural and Multidisciplinary Optimization* 60 (2019) 1283–1287.
- [9] V. Keshavarzzadeh, R. M. Kirby, A. Narayan, Stress-based topology optimization under uncertainty via simulation-based gaussian process, *Computer Methods in Applied Mechanics and Engineering* 365 (2020) 112992.
- [10] V. Keshavarzzadeh, F. Fernandez, D. A. Tortorelli, Topology optimization under uncertainty via non-intrusive polynomial chaos expansion, *Computer Methods in Applied Mechanics and Engineering* 318 (2017) 120–147.
- [11] L. W. Ng, K. E. Willcox, Multifidelity approaches for optimization under uncertainty, *International Journal for numerical methods in Engineering* 100 (10) (2014) 746–772.
- [12] J. Zheng, Z. Luo, C. Jiang, J. Wu, Level-set topology optimization for robust design of structures under hybrid uncertainties, *International Journal for Numerical Methods in Engineering* 117 (5) (2019) 523–542.
- [13] G. A. da Silva, N. Aage, A. T. Beck, O. Sigmund, Three-dimensional manufacturing tolerant topology optimization with hundreds of millions of local stress constraints, *International Journal for Numerical Methods in Engineering* 122 (2) (2021) 548–578.
- [14] R. B. dos Santos, A. J. Torii, A. A. Novotny, Reliability-based topology optimization of structures under stress constraints, *International journal for numerical methods in engineering* 114 (6) (2018) 660–674.
- [15] W. Ding, H. Liao, X. Yuan, Multi-material topology optimization considering arbitrary strength and yield criteria constraints with single-variable interpolation, *International Journal for Numerical Methods in Engineering* 125 (19) (2024) e7561.
- [16] H. Tiesler, R. M. Kirby, D. Xiu, T. Preusser, Stochastic collocation for optimal control problems with stochastic pde constraints, *SIAM Journal on Control and Optimization* 50 (5) (2012) 2659–2682.

- [17] E. Rosseel, G. N. Wells, Optimal control with stochastic pde constraints and uncertain controls, *Computer Methods in Applied Mechanics and Engineering* 213 (2012) 152–167.
- [18] A. Alexanderian, N. Petra, G. Stadler, O. Ghattas, Mean-variance risk-averse optimal control of systems governed by pdes with random parameter fields using quadratic approximations, *SIAM/ASA Journal on Uncertainty Quantification* 5 (1) (2017) 1166–1192.
- [19] P. Chen, U. Villa, O. Ghattas, Taylor approximation and variance reduction for pde-constrained optimal control under uncertainty, *Journal of Computational Physics* 385 (2019) 163–186.
- [20] P. Chen, M. R. Haberman, O. Ghattas, Optimal design of acoustic meta-material cloaks under uncertainty, *Journal of Computational Physics* 431 (2021) 110114.
- [21] J. C. Krüger, M. Kranz, T. Schmidt, R. Seifried, B. Kriegesmann, An efficient and non-intrusive approach for robust design optimization with the first-order second-moment method, *Computer methods in applied mechanics and engineering* 414 (2023) 116136.
- [22] K. Maute, Topology optimization under uncertainty, in: *Topology optimization in structural and continuum mechanics*, Springer, 2014, pp. 457–471.
- [23] D. P. Kouri, T. M. Surowiec, Risk-averse pde-constrained optimization using the conditional value-at-risk, *SIAM Journal on Optimization* 26 (1) (2016) 365–396.
- [24] D. Luo, T. O’Leary-Roseberry, P. Chen, O. Ghattas, Efficient pde-constrained optimization under high-dimensional uncertainty using derivative-informed neural operators, *arXiv preprint arXiv:2305.20053* (2023).
- [25] P. Chen, O. Ghattas, Taylor approximation for chance constrained optimization problems governed by partial differential equations with high-dimensional random parameters, *SIAM/ASA Journal on Uncertainty Quantification* 9 (4) (2021) 1381–1410.

- [26] I. Doltsinis, Z. Kang, G. Cheng, Robust design of non-linear structures using optimization methods, *Computer methods in applied mechanics and engineering* 194 (12-16) (2005) 1779–1795.
- [27] I. Doltsinis, Z. Kang, Robust design of structures using optimization methods, *Computer methods in applied mechanics and engineering* 193 (23-26) (2004) 2221–2237.
- [28] B. S. Lazarov, M. Schevenels, O. Sigmund, Topology optimization with geometric uncertainties by perturbation techniques, *International Journal for Numerical Methods in Engineering* 90 (11) (2012) 1321–1336.
- [29] M. Kranz, J. K. Lüdeker, B. Kriegesmann, A generalized approach for robust topology optimization using the first-order second-moment method for arbitrary response functions, *Structural and multidisciplinary optimization* 66 (5) (2023) 98.
- [30] B. Kriegesmann, J. K. Lüdeker, Robust compliance topology optimization using the first-order second-moment method, *Structural and Multidisciplinary Optimization* 60 (2019) 269–286.
- [31] J. Tan, D. Faghihi, A scalable framework for multi-objective pde-constrained design of building insulation under uncertainty, *Computer Methods in Applied Mechanics and Engineering* 419 (2024) 116628.
- [32] P. Chen, J. O. Royset, Performance bounds for pde-constrained optimization under uncertainty, *SIAM Journal on Optimization* 33 (3) (2023) 1828–1854.
- [33] Y. Wang, O. Sigmund, Multi-material topology optimization for maximizing structural stability under thermo-mechanical loading, *Computer Methods in Applied Mechanics and Engineering* 407 (2023) 115938.
- [34] C. Wang, B. Xu, Z. Duan, J. Rong, Stress-related topology optimization for castable design, *International Journal for Numerical Methods in Engineering* 122 (21) (2021) 6203–6233.
- [35] G. A. da Silva, A. T. Beck, O. Sigmund, Stress-constrained topology optimization considering uniform manufacturing uncertainties, *Computer Methods in Applied Mechanics and Engineering* 344 (2019) 512–537.

- [36] K. Li, G. Cheng, Structural topology optimization of elastoplastic continuum under shakedown theory, *International Journal for Numerical Methods in Engineering* 123 (19) (2022) 4459–4482.
- [37] D. M. De Leon, J. Alexandersen, J. S. O. Fonseca, O. Sigmund, Stress-constrained topology optimization for compliant mechanism design, *Structural and Multidisciplinary Optimization* 52 (2015) 929–943.
- [38] R. Zhao, J. Zhao, C. Wang, Stress-constrained multiscale topology optimization with connectable graded microstructures using the worst-case analysis, *International Journal for Numerical Methods in Engineering* 123 (8) (2022) 1882–1906.
- [39] P. Duysinx, M. P. Bendsøe, Topology optimization of continuum structures with local stress constraints, *International journal for numerical methods in engineering* 43 (8) (1998) 1453–1478.
- [40] D. Yang, H. Liu, W. Zhang, S. Li, Stress-constrained topology optimization based on maximum stress measures, *Computers & Structures* 198 (2018) 23–39.
- [41] C. Le, J. Norato, T. Bruns, C. Ha, D. Tortorelli, Stress-based topology optimization for continua, *Structural and Multidisciplinary Optimization* 41 (2010) 605–620.
- [42] C. Cheng, B. Yang, X. Wang, I. Lee, Uncertainty-oriented thermoelastic topology optimization with stress constraint, *International Journal for Numerical Methods in Engineering* 125 (10) (2024) e7441.
- [43] M. K. Oh, D. S. Lee, J. Yoo, Stress constrained topology optimization simultaneously considering the uncertainty of load positions, *International Journal for Numerical Methods in Engineering* 123 (2) (2022) 339–365.
- [44] J. Tan, U. Villa, N. Shamsaei, S. Shao, H. M. Zbib, D. Faghihi, A predictive discrete-continuum multiscale model of plasticity with quantified uncertainty, *International Journal of Plasticity* 138 (2021) 102935.
- [45] J. Tan, P. Maleki, L. An, M. Di Luigi, U. Villa, C. Zhou, S. Ren, D. Faghihi, A predictive multiphase model of silica aerogels for building envelope insulations, *Computational Mechanics* 69 (6) (2022) 1457–1479.

- [46] L. Roininen, J. M. J. Huttunen, S. Lasanen, Whittle-matérn priors for bayesian statistical inversion with applications in electrical impedance tomography, *Inverse Problems and Imaging* 8 (2) (2014) 561–586. doi:10.3934/ipi.2014.8.561.
URL <https://www.aims sciences.org/article/id/466c718a-c026-4ea2-bdd5-699793c40890>
- [47] A. Alexanderian, P. J. Gloor, O. Ghattas, On bayesian a-and d-optimal experimental designs in infinite dimensions (2016).
- [48] H. Avron, S. Toledo, Randomized algorithms for estimating the trace of an implicit symmetric positive semi-definite matrix, *Journal of the ACM (JACM)* 58 (2) (2011) 1–34.
- [49] B. Liang, J. Tan, L. Lozenski, D. A. Hormuth, T. E. Yankeelov, U. Villa, D. Faghihi, Bayesian inference of tissue heterogeneity for individualized prediction of glioma growth, *IEEE Transactions on Medical Imaging* 42 (10) (2023) 2865–2875.
- [50] H. Flath, L. Wilcox, V. Akçelik, J. Hill, B. van Bloemen Waanders, O. Ghattas, Fast algorithms for bayesian uncertainty quantification in large-scale linear inverse problems based on low-rank partial hessian approximations, *SIAM Journal on Scientific Computing* 33 (1) (2011) 407–432.
- [51] T. Bui-Thanh, O. Ghattas, Analysis of the hessian for inverse scattering problems: I. inverse shape scattering of acoustic waves, *Inverse Problems* 28 (5) (2012) 055001.
- [52] K. Willcox, O. Ghattas, B. van Bloemen Waanders, J. Hill, Hessian-based model reduction for large-scale systems with initial-condition inputs, *International Journal for Numerical Methods in Engineering* 73 (6) (2008) 844–868.
- [53] A. K. Saibaba, J. Lee, P. K. Kitanidis, Randomized algorithms for generalized hermitian eigenvalue problems with application to computing karhunen–loève expansion, *Numerical Linear Algebra with Applications* 23 (2) (2016) 314–339.
- [54] U. Villa, N. Petra, O. Ghattas, HIPPLYlib: An Extensible Software Framework for Large-Scale Inverse Problems Governed by PDEs: Part I:

Deterministic Inversion and Linearized Bayesian Inference, *ACM Trans. Math. Softw.* 47 (2) (Apr. 2021). doi:10.1145/3428447.
URL <https://doi.org/10.1145/3428447>

- [55] J. Nocedal, S. J. Wright, Quadratic programming, *Numerical optimization* (2006) 448–492.
- [56] M. S. Alnæs, J. Blechta, J. Hake, A. Johansson, B. Kehlet, A. Logg, C. Richardson, J. Ring, M. E. Rognes, G. N. Wells, The FEniCS project version 1.5, *Archive of Numerical Software* 3 (100) (2015). doi:10.11588/ans.2015.100.20553.
- [57] D. Luo, P. Chen, T. O’Leary-Roseberry, U. Villa, O. Ghattas, Soupy: Stochastic pde-constrained optimization under high-dimensional uncertainty in python, *Journal of Open Source Software* 9 (99) (2024) 6101. doi:10.21105/joss.06101.
URL <https://doi.org/10.21105/joss.06101>
- [58] P. K. Singh, K. A. Farrell-Maupin, D. Faghihi, A framework for strategic discovery of credible neural network surrogate models under uncertainty, *Computer Methods in Applied Mechanics and Engineering* 427 (2024) 117061.